



# The Nascent Milliquasar VT J154843.06+220812.6: Tidal Disruption Event or Extreme Accretion State Change?

Jean J. Somalwar<sup>1</sup> , Vikram Ravi<sup>1</sup> , Dillon Dong<sup>1</sup> , Matthew Graham<sup>1</sup> , Gregg Hallinan<sup>1</sup> , Casey Law<sup>1</sup> , Wenbin Lu<sup>2</sup> , and Steven T. Myers<sup>3</sup>

<sup>1</sup> Cahill Center for Astronomy and Astrophysics, MC 249-17, California Institute of Technology, Pasadena, CA 91125, USA; [jsomalwar@astro.caltech.edu](mailto:jsomalwar@astro.caltech.edu)

<sup>2</sup> Department of Astrophysical Sciences, 4 Ivy Lane, Princeton University, Princeton, NJ 08544, USA

<sup>3</sup> National Radio Astronomy Observatory, P.O. Box O, Socorro, NM 87801, USA

Received 2021 August 27; revised 2022 February 28; accepted 2022 March 14; published 2022 April 27

## Abstract

We present a detailed multiwavelength follow-up of the nuclear radio flare VT J154843.06+220812.6, hereafter VT J1548. VT J1548 was selected as a  $\sim 1$  mJy radio flare in 3 GHz observations from the Very Large Array Sky Survey. It is located in the nucleus of a low-mass ( $\log M_{\text{BH}}/M_{\odot} \sim 6$ ) host galaxy with weak or no past active galactic nuclei (AGN) activity. VT J1548 is associated with a slow rising (multiple year), bright mid-IR flare in the Wide-field Infrared Survey Explorer survey, peaking at  $\sim 10\% L_{\text{edd}}$ . No associated optical transient is detected, although we cannot rule out a short, early optical flare given the limited data available. Constant late-time ( $\sim 3$  yr post-flare) X-ray emission is detected at  $\sim 10^{42}$  erg s $^{-1}$ . The radio spectral energy distribution is consistent with synchrotron emission from an outflow incident on an asymmetric medium. A follow-up, optical spectrum shows transient, bright, high-ionization coronal line emission ([Fe XI]  $\lambda 6375$ , [Fe XI]  $\lambda 7894$ , [S XII]  $\lambda 7612$ ). Transient broad H $\alpha$  is also detected but without corresponding broad H $\beta$  emission, suggesting high nuclear extinction. We interpret this event as either a tidal disruption event or an extreme flare of an AGN, in both cases obscured by a dusty torus. Although these individual properties have been observed in previous transients, the combination is unprecedented. This event highlights the importance of searches across all wave bands for assembling a sample of nuclear flares that spans the range of observable properties and possible triggers.

*Unified Astronomy Thesaurus concepts:* [Tidal disruption \(1696\)](#); [Active galactic nuclei \(16\)](#); [Radio transient sources \(2008\)](#); [X-ray transient sources \(1852\)](#); [Transient sources \(1851\)](#)

## 1. Introduction

Supermassive black holes (SMBHs) at the centers of galaxies power a myriad of observable phenomena across cosmic time. The evolution of galaxies is closely linked to SMBH activity (e.g., Kormendy & Ho 2013). Active galactic nuclei (AGNs), which have actively accreting SMBHs at their centers, produce bright multiwavelength emission due to the presence of an accretion disk, and in many cases, an associated jet or outflow (Netzer 2015).

Quiescent or only weakly accreting SMBHs are challenging to study because of their dim or nonexistent emission. The recent advent of high cadence photometric and spectroscopic surveys has enabled the discovery of large samples of tidal disruption events (TDEs), which occur when a star is disrupted as it enters the tidal radius of an SMBH, given by  $R_T \sim R_*(M_{\text{BH}}/M_*)^{1/3}$  for a black hole (BH) of mass  $M_{\text{BH}}$  and a star of radius (mass)  $R_*(M_*)$  (e.g., Frank & Rees 1976; Rees 1988; van Velzen et al. 2011, 2019; Donley et al. 2002; Sazonov et al. 2021; van Velzen et al. 2021). TDEs provide a key probe of the SMBHs and nuclear regions in quiescent galaxies: among many insights, they enable measurements of the dust covering factors in quiescent galaxies, the circum-nuclear density profile, and they may provide a new method of measuring the mass of low-mass ( $\sim 10^6 M_{\odot}$ ) SMBHs (e.g., Metzger et al. 2012; Mockler et al. 2019; van Velzen et al. 2019;

Jiang et al. 2021a). They are often observed as  $10^{41-45}$  erg s $^{-1}$  X-ray transients, which decay with the mass fallback rate as a  $t^{-5/3}$  power law (e.g., Bade et al. 1996; Komossa & Bade 1999; Esquej et al. 2007). The X-rays may originate directly from an accretion disk or via material forced inward at the nozzle shock close to pericenter (e.g., Komossa & Bade 1999; Piran et al. 2015; Auchettl et al. 2017; Krolik et al. 2016).

While the landscape of TDEs in quiescent galaxies is rapidly being mapped out, the evolution of a TDE in a galaxy with a preexisting accretion disk is poorly understood (although recent simulations are gaining ground, see Chan et al. 2020). Given current knowledge, it is difficult, or in some cases impossible, to observationally differentiate between a nuclear flare caused by a TDE and one caused by an accretion state change (see Zabludoff et al. 2021, for a review of possible distinguishing characteristics). This problem is made particularly challenging because of the many remaining mysteries in accretion disk physics: the magnitude of possible state changes due to accretion disk instabilities, their occurrence rate, and their multiwavelength properties are largely unknown (see Lawrence 2018, and references therein).

Thus, nuclear flares from galaxies with preexisting accretion disks are particularly challenging to interpret. In galaxies where a preexisting accretion disk cannot be ruled out (i.e., those that are either weakly accreting or are quiescent but were accreting in the recent past), several aspects of the central SMBH and the inner few parsecs of the galaxy remain mysterious. For example, it is still not understood if, when, and how a dusty torus can form in a weakly accreting or non-accreting galaxy (e.g., Hönig & Beckert 2007; Hopkins et al. 2012).



Original content from this work may be used under the terms of the [Creative Commons Attribution 4.0 licence](#). Any further distribution of this work must maintain attribution to the author(s) and the title of the work, journal citation and DOI.

Progress in observationally mapping out the range and properties of nuclear flares from weakly accreting or recently accreting galaxies is advancing. For example, searches for transient line emission in the Sloan Digital Sky Survey (SDSS) spectroscopic survey (Strauss et al. 2002) have unveiled a class dubbed the extreme coronal line emitters (ECLEs), which show bright, high-ionization ( $\gtrsim 100$  eV) coronal emission lines (e.g., [Fe X]  $\lambda 6375$ , [Fe XIV]  $\lambda 5303$ ) (e.g., Komossa et al. 2008). These lines are excited by a transient, high-energy, photoionizing continuum and fade on  $\sim 3\text{--}5$  yr timescales (Yang et al. 2013).

Although most of the  $\sim 20$  known ECLEs are in quiescent galaxies (e.g., Komossa et al. 2008; Wang et al. 2011, 2012; Frederick et al. 2019; Malyali et al. 2021), an increasingly large subset are hosted by galaxies that lie in the gray area between strongly accreting AGN and quiescent galaxies. For example, ASASSN-18jd was a nuclear transient in a host galaxy with no clear evidence of AGN activity (Neustadt et al. 2020). Although this event had a TDE-like blue continuum and a high ratio of [Fe X] to [O III], it showed a non-monotonically declining optical light curve and a harder-while-fading X-ray spectrum that are both more typical of AGN activity. Likewise, the transient AT2019avd showed strong coronal line emission alongside TDE-like transient features (e.g., soft X-ray emission, Bowen fluorescence lines, broad Balmer emission), and is located in an inactive galaxy (Malyali et al. 2021). Its double-peaked optical light curve is characteristic of AGN activity, although some exotic TDE models could predict similar behavior (Malyali et al. 2021).

Originally, ECLEs were thought to be associated with TDEs, which can produce the requisite high-energy continuum that would only illuminate the coronal line-emitting region but not excite [O III] immediately because of light travel time effects (Wang et al. 2012). However, it is well known that AGN-like continua can produce coronal line emission since, before the discovery of ECLEs, coronal lines were most often observed from Seyfert galaxies of all types (e.g., Seyfert 1943; Penston et al. 1984; Gelbord et al. 2009).  $\sim 2/3$  of AGN across the range of activity levels show at least one coronal line in the near-IR (NIR; Riffel et al. 2006). This fraction is poorly constrained in the optical because optical coronal lines are dim in most AGN, with the brightest [Fe VII]  $\lambda 6086$  lines no more than  $\sim 10\%$  of the [O III]  $\lambda 5007$  flux (Murayama & Taniguchi 1998). An accretion state change could well replicate the ECLE phenomena.

Key evidence in understanding the possible triggers of ECLEs lies in their *multiwavelength* emission. ECLEs sometimes show transient, broad lines (FWHM  $\sim 1000\text{--}2000$  km s $^{-1}$ ), including hydrogen Balmer emission (e.g., Wang et al. 2012). ECLEs have been associated with optical/UV flares, which begin before the coronal lines appear (Palaversa et al. 2016; Frederick et al. 2019). Many ECLEs have been associated with IR flares with luminosities  $\sim 10^{42\text{--}43}$  erg s $^{-1}$ , consistent with emission from dust (e.g., Dou et al. 2016). The IR emission can fade on timescales as long as  $\sim 10$  yr (e.g., Dou et al. 2016). The radio emission from ECLEs, which can constrain the presence of a nascent jet or outflow, is practically unconstrained. Note that the relative frequency of the different multiwavelength signatures in galaxies that may have preexisting accretion disks and those that are quiescent are unknown.

More conclusive constraints on the trigger(s) of ECLEs require a large sample of events with minimal selection biases.

Searches based on evolving optical spectral features may miss objects similar to the ECLEs but with dimmer coronal line emission. The multiwavelength, transient emission from ECLEs will allow us to understand the full range of possible triggers and host properties.

In this work, we present the first radio-selected ECLE, SDSS J154843.06+220812.6, hereafter SDSS J1548. SDSS J1548 shows weak or no evidence for accretion, so we cannot confirm or exclude the presence of a preexisting accretion disk. SDSS J1548 was identified by Jiang et al. (2021b) as the host of a bright nuclear mid-IR (MIR) flare. Independently, we selected SDSS J1548 as part of our ongoing effort to compile a sample of radio-selected TDE candidates using the VLA Sky Survey (VLASS; Lacy et al. 2020). We performed an extensive follow-up campaign, during which we identified this object as an ECLE with additional broad Balmer features. It is X-ray bright, although, intriguingly, it shows no optical flare in the available data. The transient emission appears to evolve on long ( $\sim$  year) timescales.

We present multiwavelength observations of SDSS J1548 and the associated transient, which we label VT J1548+2208 (VT J1548 hereafter). In Section 2, we describe our target selection. In Section 3, we detail both the archival and follow-up observations and data reduction. In Section 4, we describe the non-transient galactic-scale properties of SDSS J1548. In Sections 5 and 6, we discuss the transient emission associated with VT J1548. Finally, in Section 7 we consider the possible origins (i.e., TDE, AGN-related activity) of VT J1548, and in Section 8 we conclude.

We adopt a standard flat  $\Lambda$  cold dark matter model with  $H_0 = 70$  km s $^{-1}$  Mpc $^{-1}$  and  $\Omega_m = 0.3$ . All magnitudes are reported in the AB system unless otherwise specified.

## 2. Target Selection

We selected VT J1548 during our search for radio-bright TDE candidates using the Karl G. Jansky Very Large Array Sky Survey (VLASS; also see Giannios & Metzger 2011 for the first discussion of the possibility of searching for TDEs as radio transients). VLASS is a full-sky, radio survey ( $\delta > -40^\circ$ , 2–4 GHz; Lacy et al. 2020). Each VLASS pointing will be observed three times. The first epoch (E1) was completed between 2017 and 2018 and the second (E2) is halfway done ( $\sim 2020$ –present). VLASS is optimal for studies of radio-emitting TDEs because it is sensitive ( $\sim 0.13$  mJy) and has a high angular resolution that allows for source localization to galactic nuclei ( $\sim 2''.5$ , with variations with decl. and hour angle).

D. Dong et al. (2022, in preparation), developed a pipeline to robustly identify radio transients with VLASS, which we used to select radio TDE candidates. We will describe the source detection and photometry in detail in that work; we provide a brief summary in Appendix A.

We selected TDE candidates as nuclear VLASS transients ( $< 3''$  from the center of a Pan-STARRS source; Chambers et al. 2016; Flewelling et al. 2020) with no archival radio detections ( $> 3''$  from a source in the NVSS or FIRST catalogs; Condon et al. 1998; White et al. 1997; Helfand et al. 2015). We inspect all crossmatches to ensure that the radio transient is located on a galaxy, rather than a star. After this initial selection, we verified that each source was nuclear using precise positions from Very Large Array (VLA) follow-up. We required the stellar mass of the host galaxy, measured using a spectral energy distribution (SED) fit (Section 4), to be

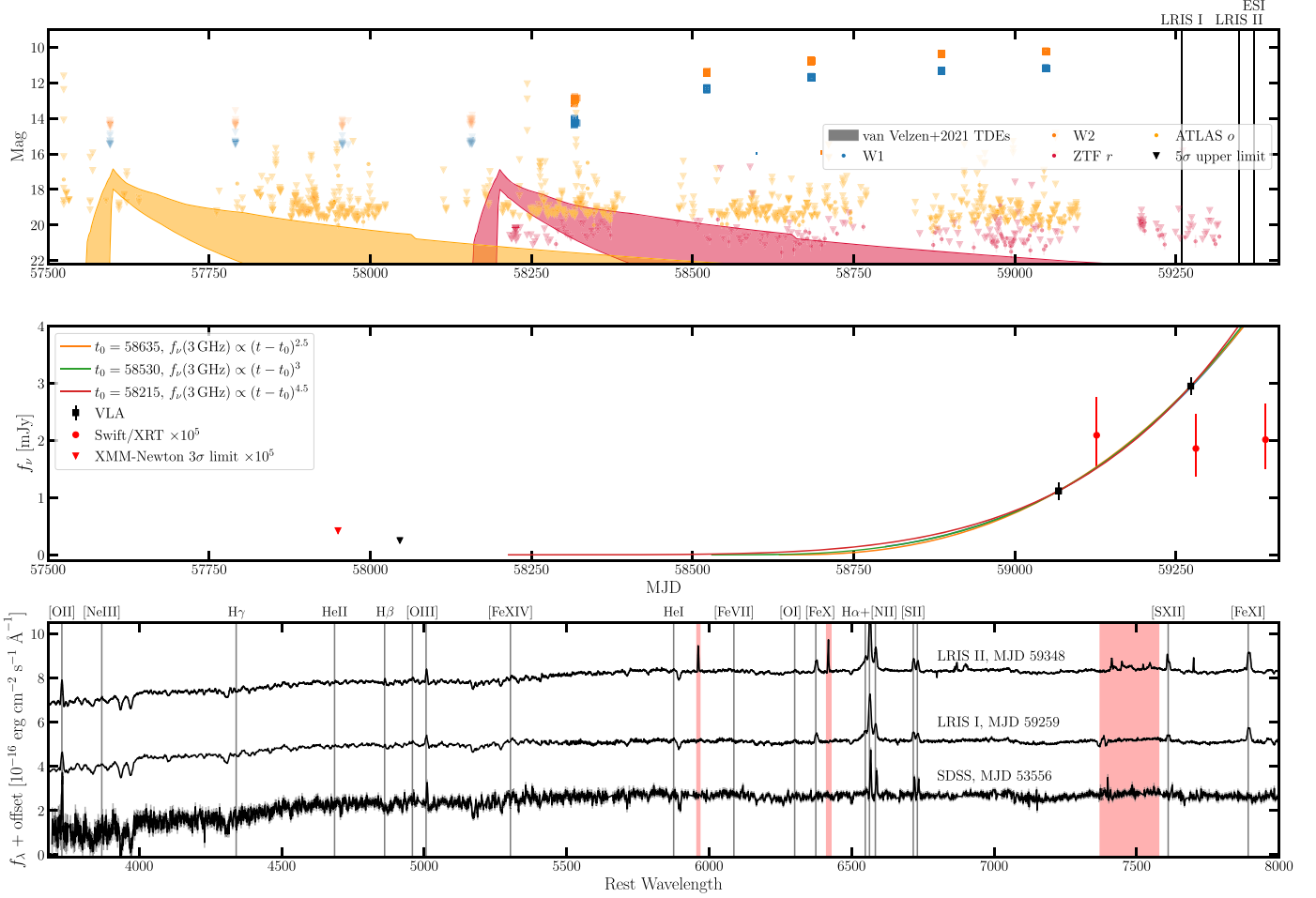


**Figure 1.** A summary of the observations of SDSS J1548. (Top panel) The optical and IR light curves for SDSS J1548. IR magnitudes are in their native Vega system, whereas optical magnitudes are in their native AB system. The IR light-curve flares by  $\sim 2\text{--}3$  mag beginning around MJD 58100. There is no obvious optical flare, although gaps in survey coverage mean that we cannot rule one out. The optical upper limits are consistent with the tail of the best-fit blackbody to the IR emission. We overplot the range of fluxes expected in different bands (as denoted by the color of the band) from typical optical TDEs as shaded regions. We have adopted the models of ZTF optical TDE light curves from Table 6 of van Velzen et al. (2021) with the appropriate distance for SDSS J1548 and extinction  $E(B-V)_{\text{nuc}} \sim 1$ . We plot the central  $\pm 1\sigma$  range of fluxes expected from these models. We shift the start date of each band to be within the coverage of the corresponding survey but still consistent with the start of the WISE flare. (Middle panel) The 3 GHz radio (black squares) and 0.2–10 keV X-ray light curves. Solid lines show power-law fits to the radio light curve, with the launch date in each case noted in the legend. (Bottom panel) The optical spectrum evolution. The late-time LRIS optical spectra show transient broad Balmer and coronal line emission. We highlight regions impacted by reduction problems in red.

consistent with  $\log M_{\text{BH}}/M_{\odot} \lesssim 8$  according to the stellar mass–SMBH mass relation from Greene et al. (2020) (i.e.,  $\log M_{*}/M_{\odot} \lesssim 12$ ). For SMBH masses  $\log M_{\text{BH}}/M_{\odot} \gtrsim 8$ , stars will be captured whole rather than be disrupted because the Hill radius is comparable to the tidal radius (Rees 1988). After this initial selection, we carefully inspected the archival radio images to ensure there are no detections (subthreshold or otherwise) that are at a position consistent with the VLASS position. We will present the full sample of radio-selected TDE candidates in future papers. In this paper, and another in preparation, we present individual, unique candidates, including VT J1548.

### 3. Observations and Data Reduction

After identifying VT J1548 as a promising TDE candidate, we performed extensive, multiwavelength follow-up. In this section, we describe the observations and data reduction. We also present the available archival data. Detailed data analysis and interpretation will be described in later sections. Figure 1 summarizes the observation time line.

#### 3.1. Radio Observations

SDSS J1548 was undetected in the NVSS and FIRST radio surveys (Condon et al. 1998; Helfand et al. 2015; White et al. 1997). Most recently, it was observed on MJD 58046 (2018 October 15) during VLASS E1 with a  $3\sigma$  upper limit  $f_{\nu}(3 \text{ GHz}) < 0.36$  mJy. VT J1548 was first detected in the radio during VLASS E2 on MJD 59068 (2020 August 7) with  $f_{\nu}(3 \text{ GHz}) = 1.12 \pm 0.15$  mJy.

We obtained a broadband (0.3–20 GHz) radio SED for VT J1548 on MJD 59273 (2021 February 28) as part of program 20B-393 (PI: Dong). We reduced the data using CASA with standard procedures. VT J1548 was detected in the *L*, *S*, *C*, and *X* bands and undetected in the *P* band.

#### 3.2. Optical/IR Light Curve

SDSS J1548 is in the survey area of the NEOWISE and Zwicky Transient Facility (ZTF) surveys (Mainzer et al. 2011; Bellm et al. 2019; Graham et al. 2019). NEOWISE has observed SDSS J1548 in the W1 ( $3.4 \mu\text{m}$ ) and W2 ( $4.6 \mu\text{m}$ )

bands with a cadence of  $\sim 6$  months since MJD  $\sim 56700$ . Each epoch consists of  $\sim 12$  exposures. We downloaded the NEOWISE photometry from [irsa.ipac.caltech.edu](http://irsa.ipac.caltech.edu). The light curve is shown in Figure 1. SDSS J1548 flared brightly in NEOWISE beginning on MJD  $\sim 58100$  (2018 March 23). It increased from W1/W2  $\sim 13.6/13.6$  mag (native Vega system) to W1/W2  $\sim 11.2/10.3$  mag (native Vega system) in  $\sim 900$  days and had not begun to fade by the most recent observation (MJD 59049; 2020 July 19). The peak flux of the flare was  $\gg 5\sigma_{\text{quies}}$ , where  $\sigma_{\text{quies}}$  was the rms variability in the pre-flare NEOWISE data.

ZTF is a high cadence optical transient survey. SDSS J1548 was observed as part of the public MSIP survey (Bellm et al. 2019), which observes the full northern sky every three nights in the *gr* filters. We used the IPAC forced photometry service (Masci et al. 2019) to download the optical light curve, and processed it using the recommended signal-to-noise cuts.<sup>4</sup> No optical transient is detected in the available data, although we may have missed the transient because of poor coverage. MJD 57500–58000 is only covered by the ATLAS survey, but the ATLAS coverage has a gap between MJD 57650 and 57750, and it is possible that an optical transient would be undetected if it occurred near 57500 and contaminated the ATLAS reference images. Assuming no systematic problems in the photometry that may mask a flare, we can exclude an optical transient that peaks during the ATLAS coverage with a flux density brighter than  $\sim 0.6$  mJy ( $L \lesssim 6 \times 10^{42}$  erg s $^{-1}$ ) at the  $5\sigma$  level in the ATLAS *o* band. This constraint rules out a flare similar to those in optically selected TDEs (van Velzen et al. 2021), unless it occurred between MJD 57650 and 57750.

### 3.3. X-Ray Observations

SDSS J1548 is not detected in any archival X-ray catalogs, including the Second ROSAT All-Sky Survey Point Source Catalog (Voges 1993; Boller et al. 2016). The best limit on the host galaxy X-ray flux is from a serendipitous 17.9 ks XMM-Newton exposure  $\sim 100$  days before the first VLASS epoch (PI: Seacrest, MJD 57950; 2017 July 16). We retrieved the Processing Pipeline System (PPS) products from the XMM-Newton archive. The PPS products have already been reduced using standard procedures with the most up-to-date pipeline and calibration files. We used the `ximage` `sosta` tool to measure the source flux at the location of SDSS J1548 on the EPIC-PN and MOS2 0.2–12 keV images (Giommi et al. 1992). (SDSS J1548 was not in the field of view of the EPIC-MOS1 image.) We used the recommended source box size. However, SDSS J1548 is near the edge of both images, so the recommended background box sizes extended off the image. We manually drew background boxes of different sizes centered on/near the source and measured the intensity in each case, to verify that our choice did not affect our result. The source was undetected, with a  $3\sigma$  upper limit on the 0.2–10 keV flux of  $\sim 10^{-13}$  erg cm $^{-2}$  s $^{-1}$ . We get a similar upper limit using both the PN and MOS1 images, which suggests that our result is not strongly affected by the fact that the source is near the image edge.

SDSS J1548 was observed three times (MJD 59127/2020 October 5; 59281/2021 March 8; 59388/2021 June 23) post-flare with  $\sim 2$  ks exposures by the Swift X-ray Telescope (Swift/XRT; Burrows et al. 2005). The final epoch was a target

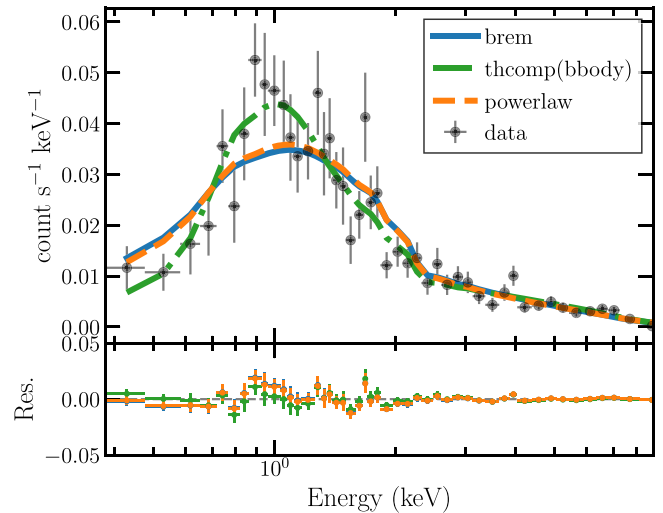


**Figure 2.** The XMM-Newton spectrum for VT J1548 (black points). The best-fit bremsstrahlung model is shown in solid blue, the best-fit Comptonized blackbody is dashed green, and the best-fit power law in dotted-dashed orange. Residuals are shown in the bottom panel. The Comptonized blackbody provides the best fit.

of opportunity (ToO) observation requested by our group. The first two observations are ToOs (PI: Dou) that we found during a search of the Swift archive. The data were reduced using the Swift HEASOFT online reduction pipeline<sup>5</sup> with default settings to generate a light curve at the position of SDSS J1548 (Evans et al. 2007). There is no significant evolution between observations.

XMM-Newton observed SDSS J1548 on MJD 59457 for a duration of 30 ks with the EPIC camera using the thin filters in full frame mode. We retrieved the PPS products and extracted a PN spectrum at the location of VT J1548 using standard procedures. The spectrum is shown in Figure 2 and we discuss it in Section 6.3.

### 3.4. Optical Spectroscopy

SDSS J1548 was observed on MJD 53556 (2005 July 5) as part of the SDSS spectroscopic survey (Strauss et al. 2002). We retrieved the archival optical spectrum from the SDSS archive. After identifying SDSS J1548 as a transient host, we observed it with the Keck I Low Resolution Image Spectrometer (LRIS; Oke et al. 1995) on MJD 59259 (2021 February 14) and 59348 (2021 May 14) with exposure times of 10 and 30 minutes, respectively. Because of poor seeing, we used the 1''.5 slit for the first epoch, but we used the 1''.0 slit for the second epoch. The slit positions are shown in Figure 3. For both epochs, we used the 400/3400 grism, the 400/8500 grating with central wavelength 7830, and the 560 dichroic. This leads to a usable wavelength range of  $\sim 1300$ –10000 Å and a resolution  $R \sim 700$ .

We reduced the first epoch of observations using the `lpipe` v2020.09 pipeline with default settings (Perley 2019). The LRIS red CCD was upgraded before the second epoch of observations and was incompatible with earlier `lpipe` versions, so we reduced this deeper epoch using `lpipe` v2021.06  $\beta$ .

We observed SDSS J1548 on MJD 59371 (2021 June 6) with the Echelle Spectrograph and Imager (ESI; Sheinis et al. 2002) on Keck II. ESI is optimal for velocity dispersion

<sup>4</sup> <http://web.ipac.caltech.edu/staff/fmasci/ztf/forcedphot.pdf>

<sup>5</sup> [https://www.swift.ac.uk/user\\_objects/index.php](https://www.swift.ac.uk/user_objects/index.php)

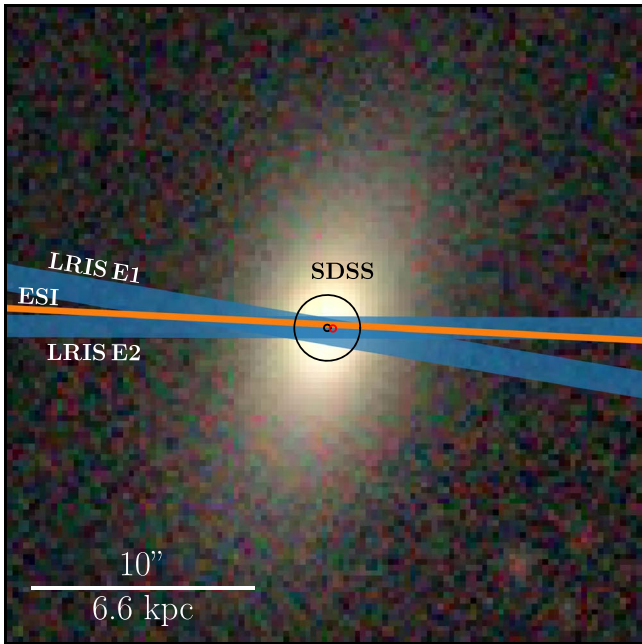


**Figure 3.** *zrg* image of SDSS J1548, the host galaxy of the radio transient VT J1548. The optical nucleus is shown as a small red circle and the radio transient position is shown as small black circle. The circle radii show approximate  $3\sigma$  statistical uncertainties. Systematic reference-frame uncertainties are not included. The radio transient is consistent with being nuclear. The blue rectangles show the slit positions for LRIS follow-up and the orange rectangles shows that for ESI follow-up. Image from the Legacy Survey (Dey et al. 2019).

measurements because of its resolution, which can be as high as  $R \sim 13,000$  ( $22.4 \text{ km s}^{-1}$  FWHM) in echelle mode. ESI in echelle mode has a wavelength coverage  $\sim 0.4\text{--}1.1 \mu\text{m}$ . We exposed for 25 minutes using the  $0.^{\prime\prime}3$  slit. The slit positioning is shown in Figure 3. We reduced the observations using the makee pipeline with the standard star Feige 34. We used default settings, except to adjust the spectral extraction aperture, as described in Appendix C.

#### 4. Host Galaxy Analysis

In this section, we describe SDSS J1548, the host galaxy of VT J1548. SDSS J1548 is at redshift  $z \sim 0.031$  ( $d_L \sim 137 \text{ Mpc}$ ). Figure 3 shows a *zrg* image of SDSS J1548. We have noted the cataloged position of the galaxy nucleus (York et al. 2000) and the radio transient position from our VLA follow-up. The radio transient is consistent with being nuclear.

SDSS J1548 is classified as an elliptical or S0 galaxy with a  $g$ -band semimajor half-light axis  $\sim 1.8 \text{ kpc}$  (Huertas-Company et al. 2011; Simard et al. 2011). It is bulge dominated, with a  $g$ - ( $r$ -) band bulge-to-disk ratio  $B/T = 0.7(0.73)$  (Simard et al. 2011). The bulge-dominated morphology is unusual for ECLEs—the known ECLEs are largely located in intermediate-luminosity disk galaxies with no apparent bulge in SDSS imaging (Wang et al. 2012).

We measured the galaxy stellar mass using an SED fit following van Velzen et al. (2021) and Mendel et al. (2014). We retrieved archival photometry from the GALEX (far-UV, near-UV; Million et al. 2016; Martin et al. 2005), SDSS (*ugriz*; Ahumada et al. 2020), and Wide-field Infrared Survey Explorer (WISE; W1, W2; Wright et al. 2010) surveys. We used *prospector* (Johnson et al. 2021), a Bayesian wrapper for the *fsps* stellar population synthesis tool (Conroy et al. 2009;

**Table 1**  
Host Galaxy

Parameter	Value
R.A.	15:48:43.06
Decl.	22:08:12.84
Redshift $z$	0.031
$d_L$	137 Mpc
$\log M_*/M_\odot$	$10.15^{+0.07}_{-0.07}$
$\log M_{\text{BH}}/M_\odot$ (from $M_{\text{BH}} - \sigma_*$ )	$6.48 \pm 0.33$

**Note.** R.A. and decl. are from the SDSS imaging survey (York et al. 2000). Redshift is as measured in our work. The stellar mass is derived from an SED fit. SMBH mass is measured using the velocity dispersion and the Kormendy & Ho (2013)  $M_{\text{BH}} - \sigma_*$  relation.

Conroy & Gunn 2010), with a Chabrier (2003) initial mass function, a  $\tau$ -model star formation history, and the Calzetti et al. (2000) attenuation curve. We fixed the redshift to the best-fit redshift from the LRIS spectrum (0.031; Appendix B). We fit the SED using the emcee Monte Carlo Chain Ensemble sampler (Foreman-Mackey et al. 2013) with 500(burn – in) + 1000 steps. The best-fit stellar mass is reported in Table 1. Our best-fit parameters are consistent with cataloged SED fits of this source from SDSS. We relate the stellar mass to the SMBH mass using the empirically derived  $M_* - M_{\text{BH}}$  relation from Greene et al. (2020). We find  $\log M_{\text{BH}} \sim 7.1 \pm 0.79$ , where the uncertainty is dominated by intrinsic scatter in the relation. Alternatively, we can relate the bulge mass to the SMBH mass using the  $M_{\text{bulge}} - M_{\text{BH}}$  relation from Kormendy & Ho (2013). We estimate the bulge mass using the bulge-to-disk ratio above, and find  $M_{\text{BH}} = 7.51 \pm 0.32$ .

The SMBH mass is more tightly correlated with the bulge velocity dispersion ( $\sigma_*$ ) than  $M_*$ . We measured  $\sigma_*$  from the high-resolution ESI spectrum and find an SMBH mass  $\log M_{\text{BH}}/M_\odot = 6.48 \pm 0.33$ , as described in Appendix C. The error is dominated by intrinsic uncertainty in the  $M_{\text{BH}} - \sigma_*$  relation. This SMBH mass is consistent with that measured by Jiang et al. (2021b) using the lower resolution archival SDSS spectrum. It corresponds to an Eddington luminosity of  $3 \times 10^{44} \text{ erg s}^{-1}$  (Gezari 2021).

Next, we constrain any prior AGN activity in SDSS J1548. The archival SDSS spectrum is shown in the bottom panel of Figure 1. It has many narrow features, including the Balmer series, [O III]  $\lambda 5007$ , [N II]  $\lambda 6548, 6584$ , and [S II]  $\lambda 6713, 6731$ , but no broad emission. We fit the narrow lines following Appendix B and the fluxes are tabulated in Table 2. Figure 4 shows five variations of the BPT diagrams, which classify galaxies according to their AGN activity (Baldwin et al. 1981; Kewley et al. 2006; Cid Fernandes et al. 2011). We plot the ECLE hosts from Wang et al. (2012) and changing look (CL) LINERs from Frederick et al. (2019), where possible. The CL LINER sample includes one ECLE (see discussion in Section 7). SDSS J1548 lies between the ECLE and CL LINER samples. It is consistent with weak or no AGN emission.

The WISE color of a galaxy (pre-transient) provides an additional constraint on its AGN activity (Assef et al. 2018). The WISE color  $W1 - W2 = 0.055$  ( $W1/W2 = 13.625 \pm 0.025 / 13.570 \pm 0.029$ ) is inconsistent with typical AGN, which have  $W1 - W2 \gtrsim 0.8$  (Assef et al. 2018). Hence, SDSS J1548 may be quiescent or weakly active. Note that the current NEOWISE color ( $W1 - W2 \sim 0.9$ ) is in the AGN regime.

**Table 2**  
Optical Emission Line Strengths

Line	SDSS	LRIS I	LRIS II
H $\alpha$ (narrow)	15.60 $^{+0.24}_{-0.35}$	16.95 $^{+2.54}_{-2.78}$	23.34 $^{+0.09}_{-0.15}$
H $\alpha$ (2060 km s $^{-1}$ )	—	18.09 $^{+3.84}_{-4.22}$	26.32 $^{+1.37}_{-1.48}$
H $\beta$	4.69 $^{+0.61}_{-0.61}$	3.88 $^{+0.50}_{-0.39}$	3.84 $^{+0.35}_{-0.31}$
[O I] $\lambda$ 6300	1.49 $^{+0.89}_{-0.37}$	1.41 $^{+0.27}_{-0.23}$	1.54 $^{+0.32}_{-0.38}$
[Fe X] $\lambda$ 6375	...	2.31 $^{+1.10}_{-1.36}$ / $2.73^{+0.64}_{-1.71}$	3.18 $^{+0.70}_{-1.01}$ / $2.56^{+0.62}_{-1.97}$
[Fe XI] $\lambda$ 7894	...	3.94 $^{+0.51}_{-0.62}$ / $4.60^{+0.40}_{-0.52}$	5.37 $^{+0.26}_{-0.44}$ / $5.50^{+0.29}_{-0.46}$
[Fe XIV] $\lambda$ 5303	...	0.65 $^{+3.31}_{-0.42}$	0.50 $^{+0.42}_{-0.30}$
[S XII] $\lambda$ 7612	...	1.73 $^{+0.31}_{-0.32}$ / $1.55^{+0.26}_{-0.42}$	2.10 $^{+0.19}_{-0.23}$ / $3.95^{+0.25}_{-0.25}$
[O II] $\lambda\lambda$ 3726, 3729	14.40 $^{+1.74}_{-2.34}$	10.23 $^{+0.59}_{-0.41}$	8.67 $^{+0.36}_{-0.43}$
[O III] $\lambda$ 4959	2.35 $^{+0.69}_{-0.44}$	1.82 $^{+0.31}_{-0.49}$	1.66 $^{+0.31}_{-0.24}$
[O III] $\lambda$ 5007	6.01 $^{+0.54}_{-0.62}$	5.69 $^{+0.48}_{-0.25}$	5.06 $^{+0.25}_{-0.25}$
[N II] $\lambda$ 6548	2.15 $^{+0.28}_{-0.54}$	1.82 $^{+0.79}_{-0.73}$	1.34 $^{+0.48}_{-0.43}$
[N II] $\lambda$ 6584	6.79 $^{+0.37}_{-0.44}$	6.57 $^{+0.48}_{-0.56}$	6.75 $^{+0.42}_{-0.39}$
[S II] $\lambda$ 6716	3.84 $^{+0.90}_{-0.53}$	4.55 $^{+0.82}_{-0.83}$	5.39 $^{+0.43}_{-1.22}$
[S II] $\lambda$ 6731	4.01 $^{+0.69}_{-0.74}$	4.51 $^{+0.81}_{-0.80}$	4.61 $^{+1.21}_{-0.38}$

**Note.** Line fluxes are reported in units of  $10^{-16}$  erg cm $^{-2}$  s $^{-1}$ . While we report absolute fluxes, the flux calibration is likely imperfect. Double-peaked lines (e.g., Fe X) have two reported fluxes which correspond to the blue and red peaks, respectively.

Finally, SDSS J1548 is within the virial radius of a small group (total halo mass  $\sim 10^{11.5} M_{\odot}$ ; Saulder et al. 2016). SDSS J1548 shows no obvious evidence for a disturbed morphology indicative of a recent interaction or merger.

## 5. Analysis of Transient Spectral Features

Next, we consider the transient emission associated with VT J1548, summarized in Figure 1. We begin by describing the transient spectral features, which will inform our discussion of the broadband emission in the next section. We identify transient lines as those present in the LRIS spectra but not in the SDSS spectrum.

First, we provide a brief summary of the transient features. The following subsections will analyze specific features in detail. The line fluxes for each observation epoch, measured using the procedure described in Appendix B, are listed in Table 2.

VT J1548 was associated with the appearance of strong, high-ionization coronal line emission. We detect [Fe X]  $\lambda$ 6375, [Fe XI]  $\lambda$ 7892, and [S XII]  $\lambda$ 7611. [Fe XIV]  $\lambda$ 5303 is marginally detected, and we do not observe any [Fe VII] emission. The coronal lines are all double peaked, with two roughly equal flux components separated by  $\sim 230$  km s $^{-1}$ . We will discuss these lines in detail in Section 5.1. We also detect a broad H $\alpha$  component (FWHM  $\sim 1900$  km s $^{-1}$ ), although we do not detect the corresponding H $\beta$  feature (Section 5.2). We refrain from a detailed line flux evolution analysis because the flux calibration may be imperfect. The transient line fluxes agree within  $2\sigma$  between the LRIS observations. The lines which are present in all observations (SDSS+LRIS) do not evolve between epochs, except that the narrow H $\alpha$  brightens. This brightening could be caused by the changing slit widths if the H $\alpha$  is extended, so we do not consider it further.

He II  $\lambda$ 4686 is commonly observed in TDE candidates accompanied by N III  $\lambda$ 4640 due to the Bowen fluorescence mechanism (Gezari 2021). We do not observe these lines.

[Fe II] lines are abundant in Seyferts but are undetected from VT J1548 (Mullaney & Ward 2008).

### 5.1. Coronal Line Emission

The strongest observed coronal lines are [Fe X]  $\lambda$ 6375 (ionization potential (IP) 262.1 eV), [Fe XI]  $\lambda$ 7894 (IP 290.9 eV), and [S XII]  $\lambda$ 7612 (IP 564.41 eV) with luminosities  $(1.2, 2.3, 1.3) \times 10^{39}$  erg s $^{-1}$ , respectively (we have summed over all velocity components, see discussion later in this section). The [O III]  $\lambda$ 5007 luminosity is  $\sim 1.2 \times 10^{39}$  erg s $^{-1}$ . The [Fe X] to [O III] ratio of  $\sim 1$  is unprecedented for *standard* Seyferts, which typically have coronal line luminosities that are a factor of  $\sim 100$  dimmer than [O III] (see Figure 5 of Wang et al. 2012). These fluxes are also marginally dimmer than observed in other ECLEs, which have  $L_{\text{Fe X, lit.}} \gtrsim 3 \times 10^{39}$  erg s $^{-1}$  despite similarly low SMBH masses (Wang et al. 2012). Selection effects may explain the brighter coronal lines in many ECLEs. Alternatively, VT J1548 may be more obscured than the Wang et al. (2012) ECLEs.

We marginally detect [Fe XIV]  $\lambda$ 5303 at  $<2\sigma$  significance. Most ECLEs with [Fe XIV]  $\lambda$ 5303 emission have  $L_{[\text{Fe XIV}]} \gtrsim 0.1L_{[\text{Fe X}]}$  (Wang et al. 2012). We expect sufficiently high-energy photons to ionize [Fe XIV] because it has a lower IP than the bright [S XII] line. Extinction could weaken the [Fe XIV] emission: [Fe XIV] is the bluest of the coronal lines. If the coronal lines are heavily extinguished, like the broad Balmer emission (see next section), the [Fe XIV] line could be extinguished by a factor of  $\sim 1.5\text{--}2$  relative to [Fe X]. This extinction is unlikely to affect the ECLE classification because reducing the [Fe X] to [O III] ratio by a factor of 10 would require  $E(B-V) \gtrsim 5$ .

We do not detect [Fe VII] emission although it has a low IP (Wang et al. 2012). There are a number of ECLEs with undetected [Fe VII], and most have been attributed to TDEs (Wang et al. 2012). These ECLEs tend to be galaxies that are less luminous and lower mass than those with detected [Fe VII], which is consistent with the low SMBH mass measured for SDSS J1548 (Wang et al. 2012). Moreover, if they are associated with an optical flare, the flare is dimmer than in those galaxies with [Fe VII] detections (Wang et al. 2012). The low statistics in current ECLE samples render these trends inconclusive.

Wang et al. (2012) suggest that [Fe VII] dim ECLEs can be explained if either the [Fe VII] is collisionally de-excited because of its low critical density ( $10^{6\text{--}7}$  cm $^{-3}$  compared to  $>10^9$  cm $^{-3}$  for the higher ionization iron lines), or if the X-ray SED is sufficiently bright and peaked above  $\sim 250$  eV so that higher ionization states are favored. The first scenario is disfavored if coronal line emission from ECLEs is produced analogously to that in Seyfert galaxies. In Seyferts, [Fe VII] is expected to be emitted from gas which is lower density and more extended than that which emits the higher ionization Fe lines. For example, Gelbord et al. (2009) suggest that the coronal line-emitting gas is embedded in a wind, and the [Fe VII] emitting gas is upstream of the gas that emits the higher ionization Fe lines. If this model also applies to ECLEs, it is unlikely that *all* of the coronal line-emitting gas is above the [Fe VII] critical density.

An excess of soft photons can cause a high [Fe X]/[Fe VII] ratio. Gelbord et al. (2009) discuss a few Seyferts with high [Fe X]/[Fe VII], which also have high [Fe X]/[O III] ratios (although not as extreme as ECLEs) and broad H $\alpha$  FWHM,

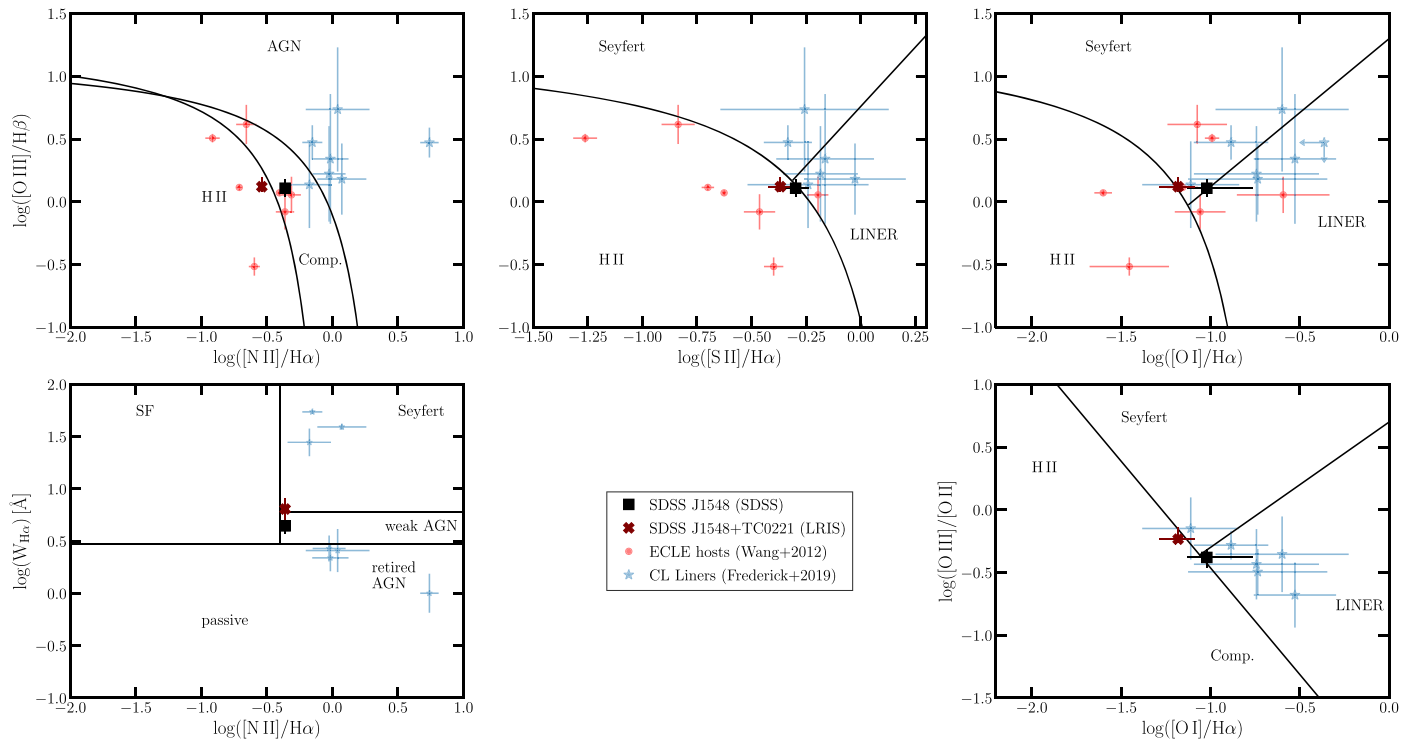


**Figure 4.** Five variations of the BPT diagram (Baldwin et al. 1981; Kewley et al. 2006; Cid Fernandes et al. 2011), following Figure 13 from Frederick et al. (2019). The SDSS measurements of SDSS J1548 are shown as a black square, while the LRIS measurements are shown as a reddish cross. Where possible, we include the changing look LINERs from Frederick et al. (2019) and the ECLEs from Wang et al. (2012) for comparison. SDSS J1548 has weak or no AGN activity.

which are narrower than expected ( $\sim 750 \text{ km s}^{-1}$ ). They argue that these extreme ratios are related to the X-ray SED shape. A soft excess which drops off around 100 eV would cause  $[\text{Fe X}]/[\text{Fe VII}]$  to be high, although it is unclear whether this would explain the extreme ratios observed in  $[\text{Fe VII}]$  dim ECLEs. Alternatively, the soft excess can continue below 100 eV if the  $[\text{Fe VII}]$  emitting gas is obscured from the photoionizing source. As Wang et al. (2012) discusses in the context of ECLEs, a very bright soft X-ray source that overionizes the coronal line-emitting gas could also explain the  $[\text{Fe VII}]$  non-detections.

Further insight into the origin of the coronal line emission comes from close inspection of the coronal line profiles in the high-resolution ESI spectrum (Figure 5). Each coronal line contains two velocity components:  $[\text{Fe X}] \lambda 6375$ ,  $[\text{Fe XI}] \lambda 7894$ , and  $[\text{S XII}] \lambda 7612$  have velocity separations of  $215 \pm 8$ ,  $240 \pm 2$ , and  $230 \pm 6 \text{ km s}^{-1}$ , respectively. These velocities are roughly consistent within uncertainties ( $\lesssim 3\sigma$  variation). The individual components all have narrow widths  $50\text{--}60 \text{ km s}^{-1}$ . From the velocity separation of the velocity components, the coronal line-emitting gas may reside at  $\sim 1 \text{ pc}$  from the SMBH, which is consistent within a factor of a few with the constraints on the position of the MIR-emitting dust, as will be described in Section 6.1.

Coronal lines in Seyferts are typically blueshifted (Gelbord et al. 2009). The blueshift is thought to indicate the ubiquitous presence of radiatively driven outflows from the AGN torus (Gelbord et al. 2009). In contrast, we observe both a red- and blueshifted component with roughly equal flux. Moreover, the line widths of coronal lines in Seyferts are often broader than the  $[\text{O III}]$  line width, whereas we observe narrower coronal line emission. No other ECLE has a published optical spectrum with sufficiently high resolution to decompose the line profiles, although the coronal lines sometimes appear non-Gaussian in

the available, low-resolution spectra (Wang et al. 2012). By eye, the published line profiles seem inconsistent with two, equal flux peaks.

The coronal line gas could be entrained in and accelerated by the synchrotron-emitting outflow (see Section 6.2), but the line widths are too narrow and the velocity difference between the components too small to favor this scenario. Alternatively, we may be observing rotating gas clouds at a radius  $\sim 1 \text{ pc}$ , corresponding to the velocity separation of the two components of the coronal lines, or an obscured, gaseous disk. The coronal line-emitting clouds could also be moving in a radiation-driven outflow, as is thought to occur in Seyferts (Gelbord et al. 2009). We tentatively favor the final scenario although, as we discussed above, the observed line profiles are different from those in typical Seyferts given that the radiatively driven outflow model has observational support in coronal line-emitting Seyferts and the different profiles could result from a different geometry. Future observations of the line profile evolution and more detailed modeling, such as was done in Mullaney et al. (2009) using CLOUDY, would constrain this scenario.

Next, we constrain the physical properties of the emitting region. We assume the emission is dominated by photoionized gas. This is a reasonable assumption because shocks only strongly contribute to coronal line emission for shock velocities  $\gtrsim 300 \text{ km s}^{-1}$ , which is much larger than the coronal line widths (Viegas-Aldrovandi & Contini 1989). Photoionized gas is expected to be at a temperature  $\sim 10^5 \text{ K}$  (Korista & Ferland 1989), so we adopt this as our fiducial value.

First, we roughly estimate the emission measure of the gas following Wang et al. (2011). Because the gas is photoionized, it must be optically thin to bound-free absorption of soft X-rays of energy  $\sim 1 \text{ keV}$ . We ignore collisional de-excitation to

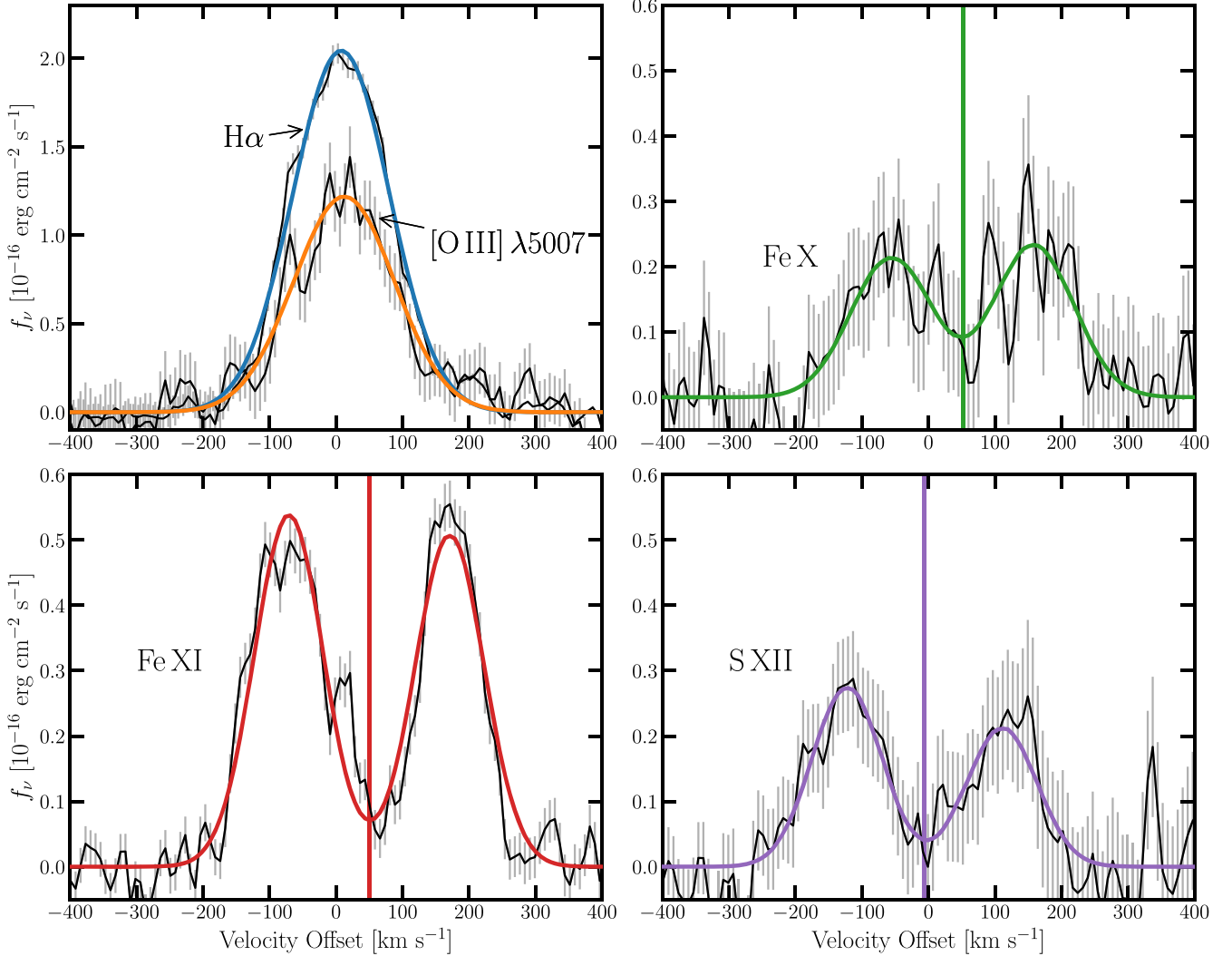


**Figure 5.** Line profiles for selected lines from the ESI observations of SDSS J1548. The top left panel shows the  $\text{H}\alpha$  narrow component and  $[\text{O III}]$  line profiles. The faint lines show the observations and the solid lines show Gaussian fits, where we include two Gaussian components in each case to match the coronal line profiles. The top right and bottom panels show the coronal line profiles, which all clearly contain two Gaussian components separated by 215–240  $\text{km s}^{-1}$ . The solid lines in between each pair of lines indicates the average of the two peak wavelengths.

simplify the calculations. For a uniform emitting region of volume  $V$  with an ion (electron) density  $n_{i(e)}$ , the emission measure is given by  $\text{EM} = n_e n_i V$ . For a given ion  $i$ , The emission measure is related to the observed line luminosity  $L_i$ :  $\text{EM} = L_i / C_i(T)$ . Here,  $C_i(T)$  is the collisional strength for the relevant ion at the gas temperature  $T \sim 10^5$  K. We retrieve the collision strengths from the CHIANTI archive (Dere et al. 1997; Del Zanna et al. 2021). We find that the emission measures for each strong coronal line are similar, with  $\text{EM}_{\text{CL}} \sim 10^{58-59} \text{ cm}^{-3}$ . Assuming the gas has solar abundances, the sulfur and iron abundances are both  $n/n_{\text{H}} \sim 10^{-5}$  (Draine 2011a). We assume both sulfur and iron are dominantly in the observed highly ionized states. Then, we can write  $n_e n_{\text{H}} V \sim n_{\text{H}}^2 V \sim 10^{64} \text{ cm}^{-3}$  and

$$V = \frac{4}{3}\pi R^3 = 10^{46} \text{ cm}^3 \left( \frac{n_{\text{H}}}{10^9 \text{ cm}^{-3}} \right)^{-2}, \quad (1)$$

$$R = 1.3 \times 10^{15} \text{ cm} \left( \frac{n_{\text{H}}}{10^9 \text{ cm}^{-3}} \right)^{-2/3}, \quad (2)$$

$$M = m_{\text{H}} n_{\text{H}} V = 8.4 \times 10^{-3} M_{\odot} \left( \frac{n_{\text{H}}}{10^9 \text{ cm}^{-3}} \right)^{-1}. \quad (3)$$

We adopt a distance  $\sim 0.8$  pc based on the coronal line widths. The coronal line-emitting gas may be at a different distance if it is outflowing, but given the low velocity we do not expect the true distance to be changed by more than a factor of a few. With this assumption, the gas must have  $R \lesssim 0.8$  pc or  $n_{\text{H}} \gtrsim 10^4 \text{ cm}^{-3}$ . The detection of [Fe X] emission requires  $n_{\text{H}} \lesssim 10^9 \text{ cm}^{-3}$ , which is the critical density of that line. This density range corresponds to  $8.4 \times 10^{-3} M_{\odot} \lesssim M \lesssim 800$ . The large mass at the upper bound leads us to favor a higher density than  $\sim 10^4 \text{ cm}^{-3}$ . The gas column density is  $10^{22} \lesssim N_{\text{H}}/\text{cm}^{-2} \lesssim 10^{24}$ .

For column densities above a few times  $10^{23} \text{ cm}^{-2}$  the gas is optically thick to X-rays. We require optically thin gas. If the gas is clumpy or in a thin shell, the column density will be scaled by a factor of  $\xi^{2/3}$ , where  $\xi = \Delta R/R$  is the relative thickness of the shell or clumps. Likewise, the radius will scale by a factor of  $\xi^{-1/3}$ . If we adopt a column density  $\sim 10^{22} \text{ cm}^{-2}$ , we find  $\xi \sim 10^{-(3-5)}$ . Thus, either the coronal line-emitting gas has a very low density but fills a large volume, which is

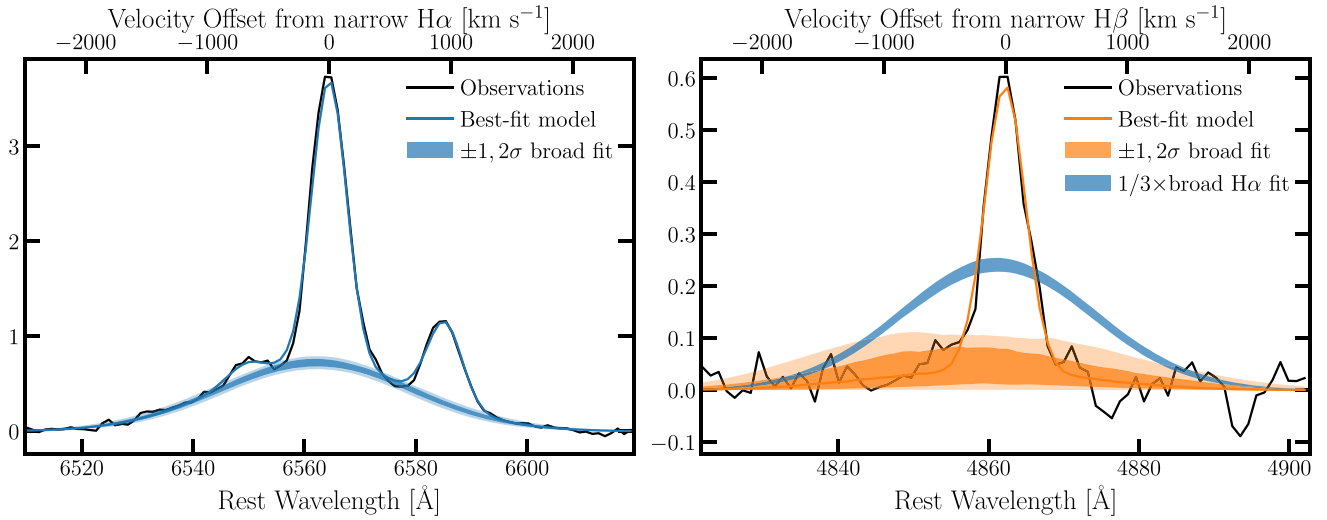


**Figure 6.** Balmer line profiles from the second epoch of LRIS observations of SDSS J1548. The left panel shows the H $\alpha$  and N II line profiles. The faint lines show the observations and the solid lines show Gaussian fits with uncertainties. A strong, broad H $\alpha$  component is clearly present. The right panel shows the H $\beta$  profile and fit. We overplot the broad H $\alpha$  fit scaled down by the expected H $\alpha$ /H $\beta$  ratio  $\sim 3$  (Dong et al. 2008). The H $\beta$  profile is inconsistent with including such a strong, broad component, suggesting that the broad emission must be heavily extinguished.

unlikely given the distinctly double-peaked, narrow-line profiles, or it is dense with a low covering factor. We favor the latter scenario.

Finally, we can constrain the soft X-ray flux required to power the coronal emission. In coronal line-emitting Seyferts, the coronal line luminosity is correlated with the flux in the soft X-ray photoionizing continuum (Gelbord et al. 2009). If we assume that ECLEs lie on this correlation, we can extrapolate to the required soft X-ray flux to power the observed coronal line emission. Given the Seyfert relation  $\log f_{\text{Fe X}}/f_X = -3.43 \pm 0.55$  (Gelbord et al. 2009), where  $f_{\text{Fe X}}$  is the flux in the [Fe X] line and  $f_X$  is the X-ray flux, we require a soft X-ray luminosity  $\sim 3 \times 10^{42}$  erg s $^{-1}$ . We will discuss the origins of this flare in more detail in Section 7.

In summary, we have detected strong, double-peaked coronal line emission (comparable to the [O III] emission). The emission likely comes from clumped gas accelerated by a radiatively driven wind or orbiting the SMBH at  $\sim 0.3$  pc. The coronal lines require an X-ray source with luminosity  $\sim 3 \times 10^{42}$  erg s $^{-1}$ , with significant uncertainty.

### 5.2. Broad Balmer Emission

VT J1548 is associated with strong, broad H $\alpha$  emission with luminosity  $\sim 4 \times 10^{39}$  erg s $^{-1}$  and width  $\sim 1900$  km s $^{-1}$  (Figure 6). The detection of late-time broad H $\alpha$  from an optical TDE is uncommon, but this luminosity and width are both consistent with upper limits on  $\sim 1000$  day H $\alpha$  emission in optical TDEs (see Figure 7 of Brown et al. 2017). The  $\sim 1900$  km s $^{-1}$  width corresponds to a radius  $\sim 5 \times 10^{-3}$  pc  $\sim 1000$  au whether the gas is orbiting the SMBH or driven in an outflow (the correspondence between the expected radius in each case is a coincidence).

The H $\alpha$  luminosity is dimmer than typical AGN emission. The Greene & Ho (2005) relationship between SMBH mass and the broad H $\alpha$  luminosity/width predicts  $\log M_{\text{BH}}/M_{\odot} \sim 5.3$  from the observed broad H $\alpha$ , which is smaller than the SMBH mass predicted by the  $M_{\text{BH}}-\sigma_*$  relation. The Greene & Ho (2005) relation was not calibrated to such low-mass BHs and this

line is heavily extinguished (see next paragraph), so we cannot exclude that the broad emission is consistent with or brighter than that from AGN.

We see no evidence for broad H $\beta$ , which is unusual for optical TDEs. In AGN broad-line regions (BLRs), the expected value of the H $\alpha$ /H $\beta$  ratio is universally  $\sim 3$  (Dong et al. 2008) so we expect an H $\beta$  luminosity  $\sim 2 \times 10^{39}$  erg s $^{-1}$ . Possible modifications to account for collisional excitation can increase the ratio to  $\lesssim 5$ , although whether these higher ratios are ever observed is debated (e.g., Ilić & Popović 2012). As shown in Figure 6, such a bright line would be detectable.

Extinction in the galactic nucleus preferentially obscures broad H $\beta$  because it is bluer than H $\alpha$ . Extinction is related to the Balmer line ratio as  $E(B-V)_{\text{nuc}} = 1.97 \log \frac{H\alpha/H\beta}{3}$ . We set an upper limit on the broad H $\beta$  flux by force fitting a Gaussian profile at the location of H $\beta$  with an FWHM constrained to be within 1 $\sigma$  of the broad H $\alpha$  FWHM. The 3 $\sigma$  lower limit on the extinction is  $E(B-V)_{\text{nuc}} > 0.7$ . Comparing to measurements of column density and dust extinction in Seyferts BLRs (Schnorr-Müller et al. 2016), we find that this corresponds to an absorbing column density  $\log N_{\text{H}}/\text{cm}^{-2} \gtrsim 21.5$ .

This extinction is similar to that observed in Seyfert 1.9 galaxies (Schnorr-Müller et al. 2016). Seyfert 1.9s are an inhomogeneous class (see Hernández-García et al. 2017, and references therein). Some fraction likely have a large torus that extinguishes the broad H $\beta$ . Galactic-scale extinction can also play a role in these Seyferts, as well as an abnormal nuclear continuum. As discussed in Section 7, we favor a torus as the cause of the high extinction in VT J1548. We cannot exclude the latter two possibilities. For example, a dust lane covering the nucleus could obscure the BLR while remaining consistent with the observed narrow Balmer decrement  $\sim 3.3$  if the narrow H $\alpha$  comes from a very extended region.

In summary, we detect broad H $\alpha$  but no broad H $\beta$ , suggesting we are observing high velocity gas near the SMBH through a screen of obscuring material.

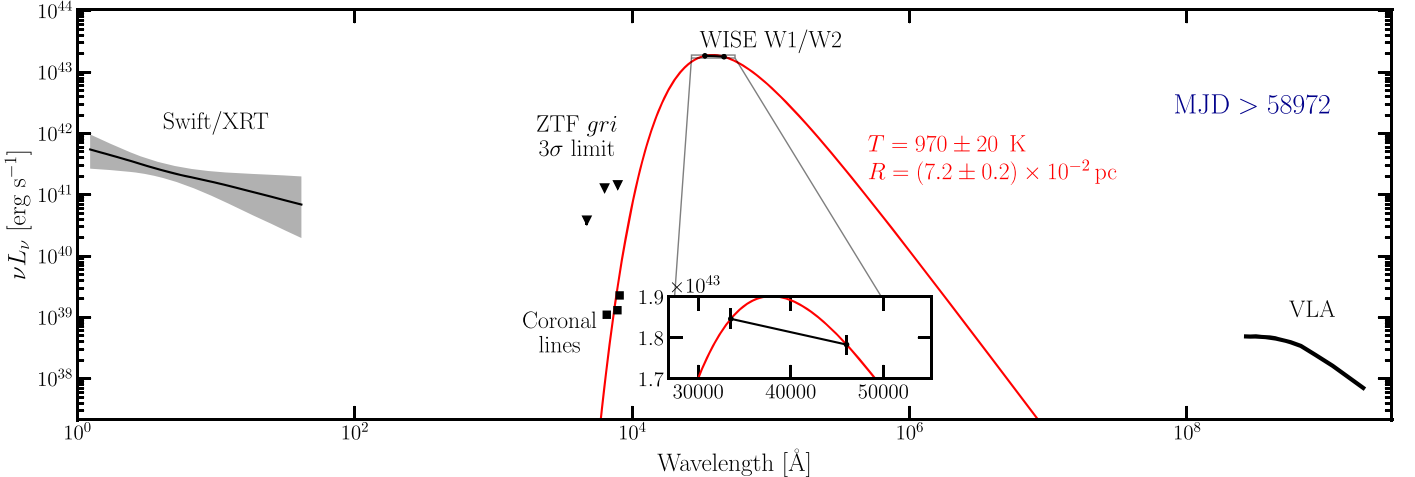


**Figure 7.** Late-time multiwavelength SED of VT J1548. We show the most recent WISE and ZTF observations, along with the VLA SED and the unabsorbed Swift/XRT best-fit spectrum. We also include the coronal line emission and the best-fit blackbody to the WISE emission. Note that the reported blackbody parameter uncertainties are only due to errors in the NEOWISE flux measurement; differential internal extinction between the WISE W1 and W2 bands could increase the temperature by  $\sim 250$  K for the extreme case  $E(B - V) = 3$ .

## 6. Analysis of Transient Broadband Features

VT J1548 was associated with flares in the infrared (Section 6.1), radio (Section 6.2), and X-ray (Section 6.3). The light curve for each flare is shown in Figure 1. VT J1548 was not detected in the optical, and we postpone discussion of the non-detection to Section 7.

### 6.1. Infrared Flare

VT J1548 is associated with a bright ( $\Delta m \sim 2$ ), long lasting ( $\gtrsim 1000$  day) flare in the WISE MIR bands. This flare was  $>5\times$  brighter than the quiescent state variability. Recent work on IR flares in galactic nuclei has largely argued that the flares can be modeled as *dust echoes* (Lu et al. 2016). Dust echoes occur when EUV photons are absorbed by circumnuclear dust and reprocessed into IR emission.

Dust echo emission can be fit using detailed models including the dust geometry and emission properties, but they typically agree closely with a blackbody fit (e.g., Kool et al. 2020). We fit a blackbody curve to the WISE data points at each epoch. Figure 7 shows the WISE SED and blackbody fit in the final epoch. We only report uncertainties due to the flux errors reported by NEOWISE. We emphasize that these uncertainties do not account for internal extinction: while extinction is small in the WISE bands, differential extinction between the W1 and W2 bands could increase the measured blackbody temperature by as much as  $\sim 250$  K for an extreme  $E(B - V) = 3$ . This shift is sufficiently small that it does not change our conclusions significantly but should be noted.

The emission plateaus at a near constant temperature  $\sim 1000$  K (Figure 8). The blackbody radius grows from  $0.7 \times 10^{-2}$  to  $7 \times 10^{-2}$  pc (although note that this radius does not correspond to the size of the emitting region but instead encodes information about the dust geometry and properties, see discussion in the rest of this section). The dust luminosity has risen to  $\sim 3 \times 10^{43}$  erg s $^{-1}$   $\sim 0.1 L_{\text{edd}}$ , and has yet to fade.

Integrating the blackbody flux, we find a lower limit on the total emitted energy  $\sim 5 \times 10^{50}$  erg. If we assume that this energy is provided by accretion with an efficiency  $\eta \sim 0.1$ , the accreted mass must be  $\gtrsim 10^{-3} M_{\odot}$ . This is consistent the energy emitted during the first few hundred days of typical TDEs,

although a factor of 10–100 more energy may be emitted on much longer timescales ( $\gtrsim 5$  yr) (see van Velzen et al. 2019, for a review).

A simple explanation of the rising light curve and nearly constant temperature is a light travel delay due to dust on different sides of the SMBH. This means that the dust is located at a distance  $\sim 1000$  day  $\times c/2 \sim 0.4$  pc from the source. We can determine the bolometric luminosity required to produce the IR radiation using the equilibrium between heating and radiative cooling:

$$e^{-\tau} \frac{L_{\text{bol}}}{4\pi R^2} \pi a^2 Q_{\text{abs}} = \langle Q_{\text{abs}} \rangle_{\text{P}} 4\pi a^2 \sigma T^4. \quad (4)$$

$\tau$  is the optical depth for absorption of the heating photons at radii  $< R$ .  $L_{\text{bol}}$  is the bolometric luminosity of the flare.  $R$  is the emitting radius and  $T$  is the emitting temperature.  $a_{\mu}$  is the grain size in units of microns.  $Q_{\text{abs}} \sim 1$  is the absorption efficiency for the incident photons (Draine 2011b), while  $\langle Q_{\text{abs}} \rangle_{\text{P}} \sim a_{\mu}(T/1000 \text{ K})$  is the Planck-averaged absorption efficiency appropriate for  $a_{\mu} \lesssim 1$  and  $500 \lesssim T/\text{K} \lesssim 1500$  (Draine & Lee 1984). Assuming a negligible optical depth  $\tau$ , we find the bolometric luminosity of the flare is  $L_{\text{bol}} \sim 10^{44}$  erg s $^{-1} \sim L_{\text{edd}}$ , assuming a grain size of  $0.1 \mu\text{m}$  (Draine & Lee 1984). The flare was due to a near- or super-Eddington episode of accretion.

Alternatively, we can estimate the bolometric luminosity required to heat the dust from the total emitted energy and rise time. The rise time of the IR emission sets an upper bound on the length of the flare that heated the dust. Given that the luminosity seemed to near a plateau or peak at MJD  $\sim 59000$  (Figure 8), the total length of the ionizing flare is probably  $\lesssim 1000$  days. The total emitted energy is  $\sim 5 \times 10^{50}$  erg s $^{-1}$ . If we assume a dust covering factor of  $\sim 1\%$ , which is typical of optically selected TDEs (van Velzen et al. 2016; Jiang et al. 2021a) we find  $L_{\text{bol}} \gtrsim 6 \times 10^{44}$  erg s $^{-1}$ . If we assume a covering factor  $\sim 10\%$ , which is consistent with an AGN torus (Ricci et al. 2017),  $L_{\text{bol}} \gtrsim 6 \times 10^{43}$  erg s $^{-1}$ . We favor a higher covering factor ( $\gtrsim 10\%$ ) given the high extinction of the BLR described in Section 5.2. Regardless of the covering factor, the UV flare that heated the dust must have been near- or

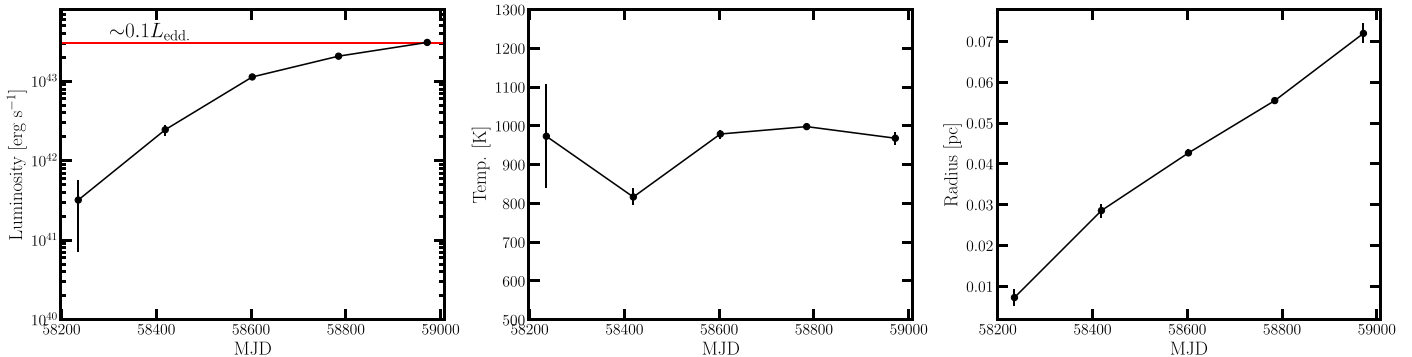


**Figure 8.** The best-fit blackbody parameters for the MIR transient associated with VT J1548. The luminosity (left panel), temperature (middle panel), and radius (right panel) evolution are shown with  $1\sigma$  uncertainties. The reported uncertainties are due to errors in the NEOWISE flux measurement. Differential internal extinction between the WISE W1 and W2 bands could increase the temperature by  $\sim 250$  K for the extreme case  $E(B - V) = 3$ .

super-Eddington. If we adopt these estimates for the bolometric luminosity and a flare length of 1000 days, the total emitted energy is  $\sim 5 \times 10^{51-52}$  erg, which is substantially higher than the lower bound discussed earlier. As before, we assume that this energy is provided by accretion with an efficiency  $\eta \sim 0.1$ , so the accreted mass is  $\sim 0.03-0.3 M_{\odot}$ . Depending on the dust covering factor, this energy may correspond to a significant fraction of the stellar mass.

In summary, VT J1548 is associated with a  $\sim 10\%$  Eddington MIR flare that has been ongoing for  $\sim 3$  yr. The MIR emission is powered by a near- or super-Eddington nuclear flare.

## 6.2. Radio Emission

In this section, we discuss the transient radio emission. First, we consider the rapid light-curve evolution. Then, we model the broadband SED.

The radio light curve is shown in Figure 1. If the radio emission turned on when the IR emission turned on, the fast rise between the VLASS E2 and VLA follow-up observations requires  $F_{\nu}(3 \text{ GHz}) \propto \Delta t^{4.5}$ . The fastest expected optically thick flux density rise is  $F_{\nu}(3 \text{ GHz}) \propto \Delta t^3$  for an on-axis, relativistic jet, which is likely an oversimplification (see discussion in Horesh et al. 2021). The observed radio emission rises as  $\Delta t^3$  if it turned on  $\sim 400$  days after the IR flare (MJD 58530). The emission is best modeled as sub-relativistic (see discussion at the end of this section), so the light curve should rise more slowly than  $\Delta t^{2.5}$ , which corresponds to an outflow launch date  $\sim 500$  days after the initial IR flare (MJD 58635). These rise times all assume a constant circumnuclear density profile, which is likely incorrect. The launch date need not be delayed if the outflow evolved for  $\sim 700$  days before colliding with a dense shell of material.

The radio SED provides insight into the unusual light-curve evolution. The observed SED, shown in Figure 9, has evolved significantly between the VLASS E2 observations (green points) and the VLA follow-up (black points). The uncertainty on the in-band slope from the VLASS E2 observations is too large to make any conclusive claims, but the 2–3 GHz slope has stayed roughly flat.

Radio emission from a TDE may result from a relativistic or sub-relativistic outflow interacting with the circumnuclear material and producing a synchrotron-emitting shock wave. We assume the emission is produced by a population of

electrons with a power-law energy distribution:

$$\frac{dN(\gamma)}{d\gamma} \propto \gamma^{-p}, \gamma \geq \gamma_m. \quad (5)$$

The index  $p$  depends on the acceleration mechanism, with typical mechanisms producing  $2 \lesssim p \lesssim 3$ . The minimum electron Lorentz factor,  $\gamma_m$ , is set by  $\epsilon_e$ , the fraction of the total energy used to accelerate electrons. Equipartition is commonly assumed:  $\epsilon_e = \epsilon_B \sim 0.1$ , where  $\epsilon_B$  is the fraction of the energy density stored in magnetic fields. The synchrotron self-absorption (SSA) model includes characteristic frequencies:  $\nu_m$ ,  $\nu_{sa}$ , and  $\nu_c$ .  $\nu_m$  is the synchrotron frequency of the minimum energy electrons.  $\nu_{sa}$  is the frequency below which emission is optically thick so SSA is important.  $\nu_c$  is the cooling frequency where the electron age is equal to the characteristic cooling time by SSA. We refer the reader to Ho et al. (2019) for a concise and clear description of SSA models and the characteristic frequencies.

Typically, the dominant absorption mechanism in TDE-driven outflows is SSA. Then, the radio flux density can be written as (Snellen et al. 1999)

$$\frac{F_{\nu}}{\text{mJy}} = K_1 \left( \frac{\nu}{1 \text{ GHz}} \right)^{2.5} (1 - e^{-\tau_{SA}}). \quad (6)$$

$$\tau_{SSA} = K_2 \left( \frac{\nu}{1 \text{ GHz}} \right)^{-(\alpha+2.5)}. \quad (7)$$

$K_{1,2}$  are normalizations characterizing the SED flux and optical depth, respectively.  $\alpha$  is the optically thin slope.  $\tau_{SSA}$  is the optical depth to SSA. We are forcing the optically thick slope to be  $5/2$ , which is expected for optically thick blackbody emission, where the blackbody temperature depends on frequency as  $\nu^{1/2}$ .

We fit this model to the observations using the dynesty dynamic nested sampler (Speagle 2020) with uninformative Heaviside priors. The best-fit SED is shown in the top panel of Figure 9, and the best-fit parameters are summarized in Table 3. The observed optically thick slope is shallower than the canonical  $5/2$ . Variations on this standard SSA model can predict slopes as shallow as 2 (Granot & Sari 2002), which is still inconsistent with our observations.

One possible modification of this model is strong free-free absorption (FFA) rather than SSA. The SED for an FFA

**Table 3**  
Best-fit Radio SED Parameters

Parameter	SSA	FFA	Inhomogeneous SSA	Multicomponent SSA
$K_1$	$0.46_{-0.02}^{+0.02}$	$9.65_{-0.3}^{+0.3}$	$1.85_{-0.08}^{+0.07}$	$1.68_{-0.27}^{+0.28}, 3.2_{-0.71}^{+0.55}$
$K_2$	$17.5_{-1.1}^{+1.2}$	$4.1_{-0.2}^{+0.2}$	$38.5_{-3.6}^{+3.9}$	$31_{-14}^{+67}, 278_{-59}^{+165}$
$\alpha$	$0.50_{-0.01}^{+0.01}$	$0.56_{-0.01}^{+0.02}$	$0.5_{-0.04}^{+0.04}$	$1.4_{-0.6}^{+1.3}, 1.06_{-0.05}^{+0.18}$
$\alpha'$	...	...	$1.35_{-0.05}^{+0.05}$	...
$\chi^2/\text{dof}$	496/78	458/78	69/77	62/74

**Note.** All fluxes are assumed to be in millijansky and frequencies in gigahertz.  $1\sigma$  uncertainties are reported. The multicomponent SSA model includes a low frequency pure power-law component that is not included in the reported fits, see text for details of the model.

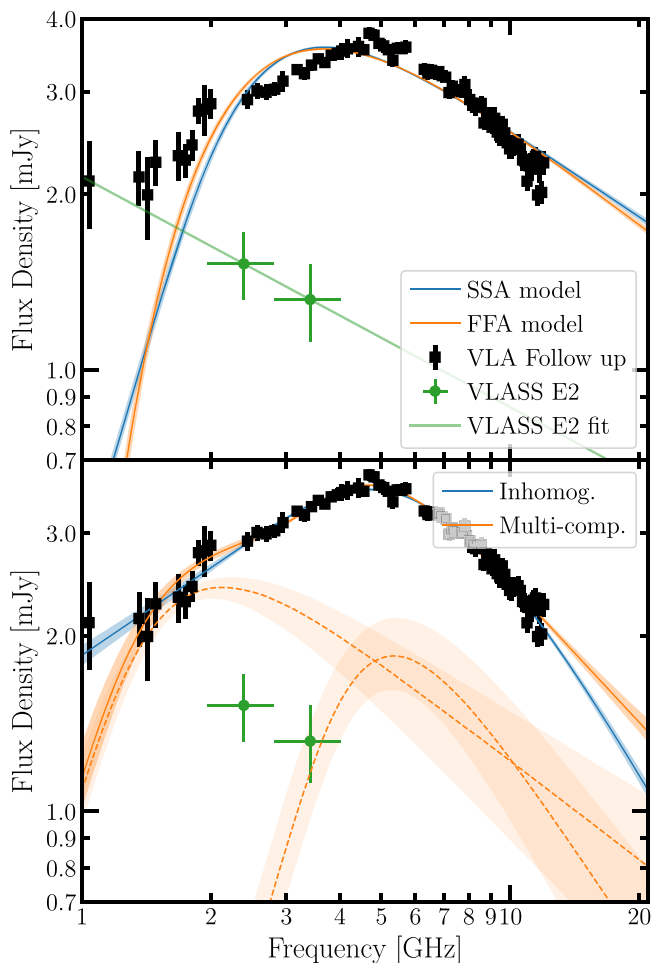


**Figure 9.** The observed radio SED and best-fit models. The top panel show the VLA follow-up observations in black, the VLASS E2 observations in green, and the best-fit self-absorbed synchrotron and free-free absorbed models, with  $1\sigma$  error bars. In both cases, the models provide extremely poor fits. We also show an extrapolation of a power-law fit to the VLASS E2 points in green. The bottom panel shows the nonstandard synchrotron model fits. The blue band shows the best-fit inhomogeneous model. The top-most orange band shows the best-fit multicomponent synchrotron model. Each component is shown as an orange band in the lower part of the panel. The nonstandard models both provide substantially better fits.

dominated model is (Chevalier 1998)

$$\frac{F_\nu}{\text{mJy}} = K_l \left( \frac{\nu}{1 \text{ GHz}} \right)^{-\alpha} e^{-\tau_{\text{FFA}}} \quad (8)$$

$$\tau_{\text{FFA}} = K_2 \left( \frac{\nu}{1 \text{ GHz}} \right)^{-2.1} \quad (9)$$

We fit this FFA model to the observations using the same techniques as for the SSA model. The best-fit parameters are tabulated in Table 3 and the model is shown in Figure 9. The fit is poor with  $\chi^2/\text{dof} = 458/78$ .

We may not be in the canonical regime with  $\nu_m < \nu_{\text{sa}} < \nu_c$  for which the above parameterizations apply. As we discuss later in this section, the magnetic fields consistent with our SED are  $\sim 0.5$  G. Assuming an emission with an age  $\gtrsim 500$  days, the corresponding cooling frequency is higher than our highest frequency observation, whereas the other two characteristic frequencies are much smaller. We tested a model with  $\nu_m < \nu_{\text{sa}} < \nu_c$ , and found that the resulting  $\chi^2$  was worse at a statistically significant level ( $p < 0.05$ ).

Instead, we must consider nonstandard emission models. First, we use a model that allows for inhomogeneities in the emitting region. Then, we consider the sum of multiple, independent SSA models.

We model an inhomogeneous emitting region following Björnsson (2013), Björnsson & Keshavarzi (2017), and Chandra et al. (2019). The probability of observing a given magnetic field is  $P(B) \propto B^{-a}$ ,  $B_0 < B < B_1$ . When the frequency is below the characteristic synchrotron frequency at  $B_0$ , the SED will have the standard optically thick slope of  $5/2$ . The slope for frequencies above the synchrotron frequency for  $B_1$  is interpreted as the optically thin slope in the standard SSA model. In between, the SED slope is  $\alpha' = (3p + 58' - a(p + 4))/(p + 2(1 + \delta'))$ , where  $0 \leq \delta' \leq 1$  characterizes a correlation between the electron distribution and the magnetic field strength distribution, and all other variables are as defined earlier. We assume the optically thick region with slope  $5/2$  is at frequencies lower than our observations, and adopt the model:

$$\frac{F_\nu}{\text{mJy}} = K_l \left( \frac{\nu}{1 \text{ GHz}} \right)^{\alpha'} (1 - e^{-\tau_{\text{SA}}}) \quad (10)$$

$$\tau_{\text{SSA}} = K_2 \left( \frac{\nu}{1 \text{ GHz}} \right)^{-[\alpha' + (p-1)/2]} \quad (11)$$

The best-fit slopes (Table 3) are  $\alpha' = 0.5$  and  $\alpha = (p-1)/2 = 1.35$ . The value of  $\alpha' = 0.5$  corresponds to  $a = 1.1, 1.6$  for  $\delta' = 0, 1$  respectively. The high frequency spectral slope corresponds to  $p \sim 3.7$ , which is substantially higher than the typical  $p < 3$ . The large  $p$  may be unphysical and suggests the inhomogeneities are more complex than assumed.

We conclude our radio SED modeling by fitting the sum of two independent SSA models. The best-fit parameters for each

**Table 4**  
Results of the Synchrotron Equipartition Analysis

Parameter	Low Freq. Comp.	High Freq. Comp.
$p$	$2.28^{+0.37}_{-0.20}$	$3.19^{+0.47}_{-0.35}$
$\log R_p \text{ cm}^{-1}$	$17.00^{+0.06}_{-0.03}$	$16.68^{+0.04}_{-0.03}$
$\log U_p \text{ erg}^{-1}$	$48.6^{+0.3}_{-0.08}$	$48.77^{+0.4}_{-0.2}$
$B_p \text{ [G]}$	$0.13^{+0.025}_{-0.009}$	$0.469^{+0.13}_{-0.08}$
$\beta$	$0.065^{+0.09}_{-0.005}$	$0.03^{+0.003}_{-0.002}$
$\log n_e \text{ cm}^{-3}$	$2.18^{+0.17}_{-0.08}$	$3.19^{+0.47}_{-0.35}$

**Note.** All parameters are derived assuming equipartition with  $\epsilon_e = \epsilon_B = 0.1$ . We assume that both the low and high frequency components correspond to outflows that launched  $\sim 700$  days after the beginning of the IR flare.

SSA profile are shown in Table 3 and the best-fit model is shown in the lower panel of Figure 9. The optically thin slopes correspond to  $p \sim 2.3/3.2$  for the low and high frequency components, respectively. Both slopes are consistent with  $2 < p < 3$  within  $1\sigma$ , so we can use a standard equipartition analysis to map the two SSA components to physical parameters of the outflow.

Chevalier (1998) provides a detailed overview of equipartition analyses. In brief, the outer radius of the shock is given by

$$R_p = \left[ \frac{6c_6^{p+5}F_p^{p+6}D^{2p+12}}{(\epsilon_e/\epsilon_B)f(p-2)\pi^{p+5}c_5^{p+6}E_l^{p-2}} \right]^{1/(2p+13)} \left( \frac{\nu_p}{2c_1} \right)^{-1}, \quad (12)$$

where the electron rest mass energy  $E_l = 0.51 \text{ MeV}$ ,  $f$  is the filling factor, and  $c_1 = 6.27 \times 10^{18} \text{ (cgs)}$ .  $c_5$  and  $c_6$  are both functions of  $p$  (Pacholczyk 1970).  $\nu_p$  is the peak frequency and  $F_p$  is the peak flux density. We have adopted the notation of Ho et al. (2019).

Assuming a time  $t_p$  since the initial event, the speed of the shock is given by  $v = \beta c \sim R_p/t_p$ . As discussed at the beginning of this section, the radio light curve for VT J1548 is inconsistent with the dominant synchrotron components corresponding to outflows that are launched with the IR flare. Hence, we calculate the launch date assuming a  $t^{2.5}$  rise, so  $t_p \sim 600$  days. A smaller  $t_p$  would result in a slightly, but not significantly, higher velocity and lower electron density.

Using the same notation, the magnetic field is given by

$$B_p = \left[ \frac{36\pi^3 c_5}{(\epsilon_e/\epsilon_B)^2 f^2 (p-2)^2 c_6^3 E_l^{2(p-2)} F_p D^2} \right]^{\frac{2}{2p+13}} \left( \frac{\nu_p}{2c_1} \right). \quad (13)$$

Here,  $D$  is the distance to the source (137 Mpc for SDSS J1548).

Finally, the equipartition energy, which is a lower bound on the true energy, is

$$U = \frac{1}{\epsilon_B} \frac{4\pi}{3} f R^3 \left( \frac{B^2}{8\pi} \right) \quad (14)$$

The physical parameters for each component are listed in Table 4. Both components are consistent with an energetic, non-relativistic outflow moving through a dense medium. The

lower frequency component, which dominates the fast-rising light curve, is faster, at slightly larger radius, and is consistent with a lower density than the higher frequency, subdominant component.

These observations might suggest that the outflow is colliding with an asymmetric and/or inhomogeneous medium. We will discuss this interpretation in Section 7. In principle, it should be possible to devise a more realistic synchrotron model that includes a physically motivated parameterization of the circumnuclear medium, but such an analysis is beyond the scope of this paper.

To conclude, VT J1548 shows fast-rising, radio emission that is consistent with an outflow at a radius  $\sim 0.1$  pc that is incident on a inhomogeneous medium.

### 6.3. X-Ray Emission

Finally, we consider the X-ray emission associated with VT J1548. First, we discuss the X-ray spectrum and luminosity. Then, we consider the source of the X-ray emission.

As shown in the middle panel of Figure 1, the X-ray emission from SDSS J1548 is bright, with an XMM-Newton flux  $\log f_\nu (0.3-10 \text{ keV})/\text{erg s}^{-1} \text{ cm}^{-2} = -12.392 \pm 0.023$ , or  $L_X = (9.5 \pm 0.5) \times 10^{41} \text{ erg s}^{-1}$ , adopting the best-fit model that will be described shortly. This is  $\sim 1\% L_{\text{Edd}}$ , and is bright compared to most late-time ( $\gtrsim 5$  yr) TDE X-ray detections but probably consistent with  $\sim 1000$  day TDE observations provided that there is ongoing accretion years to decades after the event (Jonker et al. 2020). The observed luminosity is comparable to that required by the coronal lines, so it likely powers the high-ionization emission. Assuming the X-ray flare has lasted for the same duration as the WISE flare, the total energy output is  $\sim 10^{50} \text{ erg}$ .

X-rays can also be emitted by the tail of the radio synchrotron emission. Given the likely presence of a cooling break between the X-ray and radio frequencies, the synchrotron tail underpredicts the observed X-ray emission by orders of magnitude (left panel of Figure 10). Synchrotron emission is not a significant contributor to the X-ray luminosity. The X-ray flare could be related to normal AGN variability, in which case VT J1548 should lie on the fundamental plane for BHs. In the right panel of Figure 9, we show the fundamental plane from Gültekin et al. (2019) with our observations overplotted. This source is inconsistent with accretion-related emission. Hence, it is unlikely the result of normal (non-extreme) AGN variability.

Inverse Compton scattering of radiation by electrons in the outflow can produce X-rays. In general, the ratio of synchrotron to inverse Compton power is given by

$$\frac{P_{\text{synch}}}{P_{\text{compt}}} = \frac{U_B}{U_{\text{ph}}}, \quad (15)$$

where  $U_{\text{ph}}$  is the photon energy density and  $U_B$  is the magnetic field energy density. The magnetic field in the outflow is  $\sim 0.5 \text{ G}$ , so the magnetic energy density is  $B^2/(8\pi) \sim 0.01 \text{ erg cm}^{-3}$ . The IR luminosity is  $\sim 10^{43} \text{ erg s}^{-1}$  and is emitted from a radius  $\sim 0.4$  pc. Then, we can set a lower limit on the photon energy density of  $\sim 10^{43} \text{ erg s}^{-1} \times (0.4 \text{ pc})/c \times (4/3\pi(0.4 \text{ pc})^3)^{-1} \sim 10^{-4} \text{ erg cm}^{-3}$ . Thus, we have  $P_{\text{synch}}/P_{\text{compt}} \sim 100$ . The predicted X-ray luminosity from inverse Compton scattering in the outflow is thus  $\sim 10^{36} \text{ erg s}^{-1}$ . This is  $\sim 6$  orders of magnitude lower than observed.

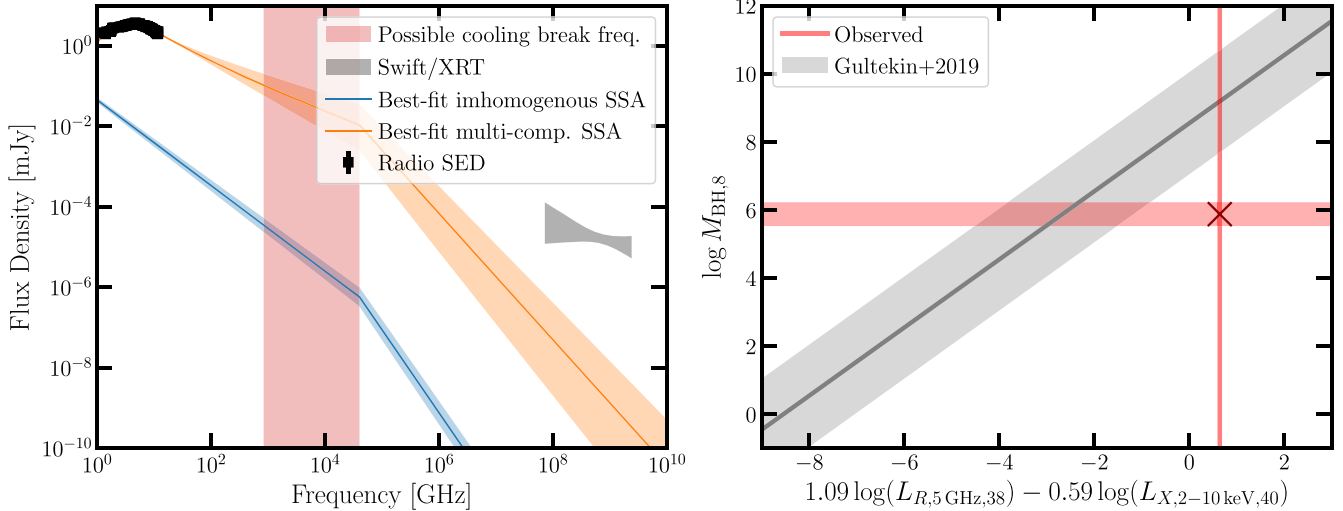


**Figure 10.** (Left panel) The radio SED compared with the observed X-ray emission. The inhomogeneous (blue) and multicomponent (orange) SSA models both predict an X-ray flux that is many orders of magnitude lower than the observations. We have included a cooling break, and the plausible cooling break frequencies are denoted by the red band. The cooling break would have to be at a frequency orders of magnitude higher than predicted for the X-ray synchrotron to be observable. We conclude that it is unlikely that the synchrotron tail contributes to the X-ray emission. (Right panel) The fundamental plane for BH accretion from Gultekin et al. (2019), with observations of SDSS J1548 overplotted. This source is inconsistent with both the X-ray and radio emission being associated with normal accretion.

**Table 5**  
Best-fit X-Ray Model Parameters

Model	$kT$ (keV)	$\Gamma$	$n_{\text{H}}$ ( $10^{22} \text{ cm}^{-2}$ )	$\log \frac{f_{\nu}(0.3-10 \text{ keV})}{\text{erg s}^{-1} \text{cm}^{-2}}$	$\chi^2/\text{dof}$
Bremmstrahlung	$25 \pm 11$	...	$0.177 \pm 0.038$	$-12.396 \pm 0.053$	74.11/43
Power law	...	$1.44 \pm 0.082$	$0.226 \pm 0.046$	$-12.394 \pm 0.023$	72.86/44
Comptonized blackbody	$0.16 \pm 0.032$	$1.17 \pm 0.16$	$0.58 \pm 0.19$	$-12.392 \pm 0.023$	51.87/42

**Note.** Best-fit X-ray model parameters. The parameters are as defined in the text.

To tightly constrain the origin of the X-rays, we model the X-ray spectrum. We use `xspec` with Cash (1979) statistics and the Wilms et al. (2000) abundances. We include both external extinction, and internal extinction within the host galaxy. We report the results for three models: bremmstrahlung (`cflux*TBabs*zTBabs*brem`), a power law (`cflux*TBabs*zTBabs*powerlaw`), and a Comptonized blackbody (`cflux*TBabs*zTBabs*thcomp(bbody)`). We have tested other simple models, including a pure blackbody, and found that they do not provide adequate fits. The bremmstrahlung model has free parameters of total 0.3–10 keV flux, internal  $n_{\text{H}}$  and temperature  $kT$ . The power-law model has free parameters of total 0.3–10 keV flux, internal  $n_{\text{H}}$  and photon index. The Comptonized blackbody model has free parameters of total 0.3–10 keV flux, internal  $n_{\text{H}}$ , blackbody temperature  $kT$ , covering fraction  $f_{\text{cov}}$ , which parameterizes the fraction of photons that are Comptonized, and the low-energy power-law photon index  $\Gamma$ . The Comptonized blackbody model also includes a high-energy cutoff, parameterized by the electron temperature  $kT_e$ , but our data do not extend to sufficiently high energies to constrain this parameter, so we fix it to the arbitrary high value  $kT_e = 150$  keV. This choice does not affect our results. The results are summarized in Table 5, and the models are shown in Figure 2.

The Comptonized blackbody model provides a statistically consistent fit that is significantly better than any of the other models tested. The temperature is consistent with X-ray loud TDEs (Sazonov et al. 2021). The intrinsic column density is  $n_{\text{H}} \sim 6 \times 10^{21} \text{ cm}^{-2}$ , similar to the column densities suggested by the coronal lines.

Hence, we conclude that the  $\sim 10^{42} \text{ erg s}^{-1}$  X-ray emission likely originates from the same source that is causing the coronal line emission and IR flare. As we discuss in the next section, the exact origin of this emission depends on the event that caused the transient. One explanation that could apply in both a TDE scenario or extreme AGN variability is AGN-like soft X-rays from an accretion disk with a hot electron corona, or emission from the base of a nascent jet, and this suggestion is supported by our measurements of the X-ray spectral shape.

## 7. Discussion

In this section, we consider models that explain the emission from VT J1548. First, we summarize the observations of SDSS J1548/VT J1548. Then, we compare VT J1548 to published transients. We present a qualitative cartoon model describing the geometry of the system. Finally, we discuss the possible events that triggered the onset of VT J1548, and we finish by describing observations that could distinguish between these properties and/or clarify our physical model.

The observational properties of VT J1548 and its host, SDSS J1548, can be summarized as follows:

1. SDSS J1548 is a bulge-dominated S0 galaxy. It has line ratios that are marginally consistent with an AGN-like ionizing source. It hosts a low-mass black hole, with  $\log M_{\text{BH}}/M_{\odot} = 6.48 \pm 0.33$ .
2. VT J1548 is associated with strong ([Fe X]/[O III]  $\sim 1$ ), double-peaked ( $\Delta v \sim 230 \text{ km s}^{-1}$ ) coronal line emission

- powered by X-ray emission with a luminosity  $\gtrsim 10^{42}$  erg s $^{-1}$ .
3. VT J1548 coincided with the onset of broad H $\alpha$  emission (FWHM  $\sim 1900$  km s $^{-1}$ ), but no broad H $\beta$  emission, suggesting strong internal extinction with  $E(B - V) \gtrsim 0.7$ .
  4. The transient emission lines commonly associated with optically selected TDEs (He II, N III) are undetected. We do not detect any of the [Fe II] lines that are abundant in Seyfert spectra.
  5. VT J1548 is associated with a bright ( $\Delta m \sim 2 - 3$ ) MIR flare. The flare rose over  $\sim 900$  days and had not begun fading from a luminosity of  $\sim 0.1L_{\text{edd}}$ , as of MJD 59000. The flare temperature stayed roughly constant at 1000 K, and the emission is consistent with dust heated by near- or super-Eddington UV flare.
  6. VT J1548 was undetected in the radio shortly before the beginning of the IR flare, but had turned on within  $\sim 2$  yr. The radio emission from VT J1548 is currently consistent with an inhomogeneous SSA model or a two-component SSA model peaking at a frequency of 5 GHz with a flux density 4 mJy, although the best-fit parameters for the two-component model are more consistent with theoretical expectations for synchrotron sources. The best-fit parameters suggest the components are both non-relativistic outflows, one of which is slightly faster with a lower electron density and magnetic field.
  7. The transient X-ray emission ( $f_X = (4.1 \pm 0.2) \times 10^{-13}$  erg cm $^{-2}$  s $^{-1}$ ,  $L_X \sim 10^{42}$  erg s $^{-1}$ ,  $kT = 0.16 \pm 0.032$  keV) is most likely produced by a Comptonized blackbody, such as would be observed from an AGN.

### 7.1. Comparison to Published Transients

These general features have individually been observed in previous transients, but never together. In this section, we compare VT J1548 to select transients from the literature. We refer the reader to Zabludoff et al. (2021) for a more comprehensive discussion of unusual TDE candidates. In Table 6, we summarize critical properties of VT J1548 and compare them to the *unusual* TDE candidates and two unique changing look AGN that we discuss in Section 7.5. We selected these transients as those that evolve in the optical/IR/X-ray on a timescale slower than the typical TDE ( $\gtrsim 400$  days) or those that initially evolve on shorter timescales but have late-time ( $>400$  day) X-ray detections. In the rest of this section, we highlight some of the unusual transients.

First, tens of ECLEs have been observed with coronal line luminosities that are generally a factor of a few higher than that observed from VT J1548 (e.g., Komossa et al. 2008; Wang et al. 2011, 2012; Frederick et al. 2019). High extinction in SDSS J1548 could cause the dim emission. The line profiles from ECLEs have not been studied in detail due to a lack of high-resolution follow-up, but double-peaked profiles are not unprecedented for normal AGN and are generally attributed to a partially obscured rotating disk or an outflow (e.g., Mazzalay et al. 2010; Gelbord et al. 2009). It would be unsurprising if high-resolution observations of ECLEs uncovered complex line profiles (see Wang et al. 2012, for a discussion of possible unusual coronal line profiles in ECLEs).

Most ECLEs are inconsistent with past AGN activity, whereas SDSS J1548 has line ratios that could be consistent with weak AGN activity (Wang et al. 2012). One exception is

AT2019avd (Frederick et al. 2021; Malyali et al. 2021), which was selected as an X-ray and optical transient in a galaxy with a low SMBH mass  $\log M_{\text{BH}}/M_{\odot} \sim 6.3 \pm 0.3$ . Like VT J1548, the host galaxy was consistent with weak or no AGN activity based on archival X-ray non-detections and BPT line ratios. The optical light curve was initially similar to standard, prompt TDE emission (i.e., it evolved over a timescale of  $\sim 100$  days), but it rebrightened significantly  $\sim 500$  days after the initial peak. Its X-ray emission was very soft ( $\Gamma \sim 5$ ) and the X-ray luminosity  $\sim 600$  days post-optical peak remained at  $\sim 10^{43}$  erg s $^{-1}$ , or  $\sim 0.1L_{\text{edd}}$ . It was detected as a WISE flare that turned on after the optical emission. An optical spectrum near the first optical peak showed Fe II emission, and another spectrum taken  $\sim 450$  days post-peak showed He II and Bowen fluorescence lines. It showed broad transient Balmer emission and a Balmer decrement close to the expected value of 3. AT2019avd has been interpreted as either an AGN flare or an unusual TDE. While the high Eddington ratio and MIR detection are similar to our observations of VT J1548, VT J1548 did show a highly extincted and showed slower evolution in the MIR. Both of these differences could be caused by a larger dusty torus in VT1548 if it is undergoing the same type of flare as AT2019avd.

There is a growing population of transients that evolve on longer timescales than the typical TDE. PS1-10adi (Kankare et al. 2017) was interpreted as a TDE candidate or highly obscured supernova in a Seyfert galaxy (Kankare et al. 2017). This event was notable for its high bolometric luminosity ( $\sim 10^{52}$  erg s $^{-1}$ ) and slow evolution: the optical light curve faded slowly over  $\sim 1000$  days after peaking at the Eddington luminosity. Kankare et al. (2017) proposed that it is a member of a class of similar transients; here, we focus on PS1-10adi for simplicity. PS1-10adi also produced a dust echo, although the dust echo faded more quickly than that of VT J1548 and followed the expected blackbody temperature evolution. It was X-ray dim until  $\sim 1500$  days, at which point it brightened in the X-rays to  $\sim 10^{43}$  erg s $^{-1}$  and rebrightened briefly in the optical/IR. PS1-10adi was not detected in the radio at early times, but without further follow-up we cannot exclude late-time rebrightening. PS1-10adi also did not show strong coronal lines. Thus, VT J1548 and PS-10adi are similar in their high Eddington ratio, slow timescales, dust echoes, and late-time X-ray detections, but there were clearly significant differences between this event and VT J1548. Some, but not all, of the differences can be explained if VT J1548 is observed on a more heavily obscured line of sight.

PS1-10adi shows properties that are similar to the class of slowly evolving flares reported by Trakhtenbrot et al. (2019b). That work focused on AT2017bgt, a slowly evolving (timescale  $\gtrsim 14$  months) optical/X-ray transient in an AGN (identified via archival X-ray detections) with  $\log M_{\text{BH}}/M_{\odot} \sim 7$ . It showed strong, broad He II and Bowen fluorescence lines, as well as broad Balmer lines. Trakhtenbrot et al. (2019b) proposed that this source, along with the similar transients OGLE17aa and that hosted by the galaxy F01004-2237, form a new class of AGN flares where the UV/optical continuum emission increases by a factor  $\sim 2$  in a few weeks. The flare in F01004-2237 was associated with a bright IR flare with  $\sim$ constant temperature that rose over thousands of days. Given the large number of similarities with VT J1548, it is feasible that VT J1548 is a member of this class but with a larger amount of dust and/or a

**Table 6**  
Comparison to Select Published Transients

Name	$\log \frac{M_{\text{BH}}}{M_{\odot}}$	BPT	$\frac{L_{\text{peak}}}{L_{\text{edd.}}}$	Optically Dim	Slow Evolution ?	MIR ?	Late-time X-Ray?	Radio ?	Delayed Radio?	ECLE?	Broad Balmer ?	$E(B - V)_{\text{nuc.}} \gtrsim 0.3?$	Trigger
AT2018dyk <sup>1</sup>	5.5	LINER	0.004	×	✓	✗	?	✗	?	✓	✓	✗	AGN/TDE
PS16dtm <sup>2,3</sup>	6	NLSy1	2.8	✗	✓	✓	?	✗	?	✗	✓	✗	AGN/TDE
SDSS J1657+2345 <sup>4</sup>	6.2	AGN	1.7	✓	✓	✓	?	?	?	✗	✓	✓	AGN/TDE
AT2019avd <sup>5,6</sup>	6.3	Comp.	0.1	✗	Double peaked	✓	?	?	?	✓	✓	✗	AGN/TDE
NGC 3599 <sup>7</sup>	6.4	Sey.2 LINER	0.004	✓	✓	?	✗	?	?	✗	✗	...	AGN/TDE
VT J1548	6.48	Comp.	0.1	✓	✓	✓	✓	✓	✓	✓	✓	✓	AGN/TDE
PS1-10adi <sup>8,9</sup>	7	H II	~1	✗	✓	✓	✓	?	?	✗	✓	?	TDE/SN
ASASSN-15oi <sup>10–12</sup>	7.1	H II	0.15	✗	✗	✗	✓	✓	✓	✗	✗	...	TDE
1ES 1927+654 <sup>13</sup>	7.3	AGN	0.01–0.2	✗	✗	?	✓	?	?	✗	✓	✓	AGN/TDE
AT2017bgt <sup>14</sup>	7.3	Comp.	≥0.1	✗	✓	?	✓	?	?	✗	✓	?	AGN/TDE
F01004-2237 <sup>15,16</sup>	7.4	H II Sey.2	0.02–0.7	✗	✓	✓	?	✗	?	✗	✗	...	AGN/TDE
OGLE17aa <sup>17</sup>	7.4	?	0.01	✗	✓	✓	?	✗	?	✗	✓	?	AGN/TDE
ASASSN-18jd <sup>18</sup>	7.6	Comp.	0.09	✗	✓	✓	✗	?	?	✓	✓	✗	AGN/TDE
XMM-L2 J1446 <sup>19</sup>	7.8	H II	0.02	✓	✓	?	✓	✗	?	✗	✗	...	AGN/TDE
ASASSN-20hx <sup>20</sup>	7.9	LLAGN?	0.003	✗	✓	?	?	?	?	✗	✗	...	AGN/TDE
WISE J1052+1519 <sup>21</sup>	8.6	AGN	0.02	✗	✓	✓	✗	?	?	✗	✓	✗	AGN fading
ASASSN-15lh <sup>11,22,23</sup>	8.7	LINER	0.1	✗	Double peaked	✓	✓	✗	✗	✗	✗	–	SN/TDE
013815+00 <sup>24</sup>	9.3	AGN	0.02	✗	✓	?	?	✓	✗	...	...	...	AGN
(Broad Mg II)													

16

**Note.** See text for further description of select transients. Transients are sorted according to SMBH mass. SMBH masses are as reported by the authors, although we prefer to report those measured using the  $M_{\text{BH}}-\sigma_*$  relation. Late-time detections refer to detections  $\sim 400$  days after the initial flare. Slow evolution refers to flares that rise over timescales  $\gtrsim 50$  days or fade over a characteristic timescale  $\gtrsim 400$  days in the optical, IR, or X-ray. Eddington ratios are very approximate; they are reported using the peak bolometric luminosity when possible, otherwise using the peak luminosity in any given wave band. The trigger is as given in the relevant reference. Question marks refer to values for which we could not find a reported measurement. Note that WISE J1052+1519 is a fading CL AGN. References: <sup>1</sup> Frederick et al. (2019), <sup>2</sup> Blanchard et al. (2017), <sup>3</sup> Jiang et al. (2017), <sup>4</sup> Yang et al. 2019, <sup>5</sup> Frederick et al. (2021), <sup>6</sup> Malyali et al. (2021), <sup>7</sup> Saxton et al. (2015), <sup>8</sup> Kankare et al. (2017), <sup>9</sup> Jiang et al. (2019), <sup>10</sup> Horesh et al. (2021), <sup>11</sup> Jiang et al. (2021a), <sup>12</sup> Holoiu et al. (2016), <sup>13</sup> Trakhtenbrot et al. (2019a), <sup>14</sup> Trakhtenbrot et al. (2019b), <sup>15</sup> Tadhunter et al. (2017), <sup>16</sup> Dou et al. (2017), <sup>17</sup> Gromadzki et al. (2019), <sup>18</sup> Neustadt et al. (2020), <sup>19</sup> Saxton et al. (2019), <sup>20</sup> Hinkle et al. (2021), <sup>21</sup> Stern et al. (2018), <sup>22</sup> Leloudas et al. (2016), <sup>23</sup> Margutti et al. (2017), <sup>24</sup> Kunert-Bajraszewska et al. (2020).

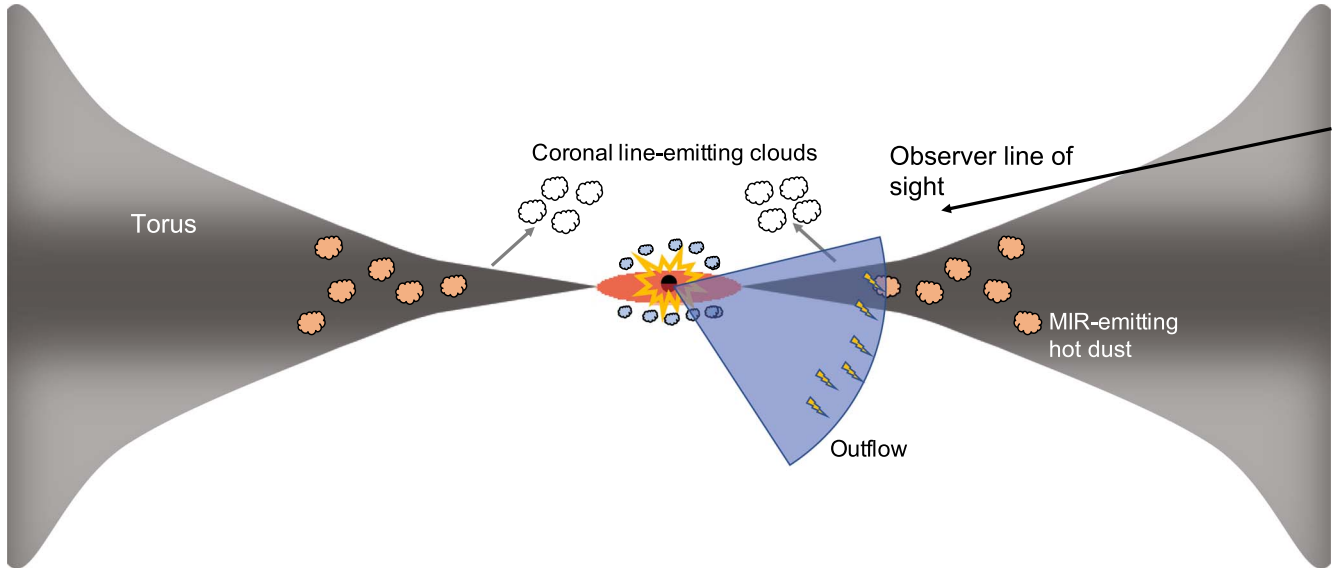


**Figure 11.** A cartoon showing the approximate geometry of SDSS J1548/VT J1548. Some event triggered a flare at the nucleus of the galaxy, which caused the formation of an accretion disk or was associated with enhanced accretion from a preexisting accretion disk. The broad H $\alpha$  emission originates from near the accretion disk ( $\sim 1000$  au), and is extinguished by the dusty torus along the line of sight to the observer. Any optical emission from the transient event is also heavily extinguished. The coronal line-emitting gas, synchrotron-emitting outflow, and MIR-emitting dust are all at roughly the same distance ( $\sim 0.4$  pc). The coronal line-emitting clouds are embedded in a radiation-driven wind ( $\sim 100$  km s $^{-1}$ ) off of the torus, which causes the double-peaked emission. Alternatively, the clouds may be orbiting the SMBH at  $\sim 0.3$  pc to produce the double-peaked lines. IR emission comes from the heated dust in the torus. The radio-emitting outflow is shown in blue.

more extincted sight line. Radio observations of AT2017bgt and like events are critical for assessing this interpretation.

Every transient discussed thus far has been detected in the optical. On the other hand, the candidate TDE or AGN flare SDSS J1657+2345 was discovered as a MIR flare with no optical counterpart (Yang et al. 2019). It evolved over  $\sim 1000$  day timescales, like VT J1548. Broad H $\alpha$  is detected in its spectrum, but no broad H $\beta$  is detected. In contrast to VT J1548, no coronal line emission is detected. Follow-up radio and X-ray observations would help determine whether this event is analogous to VT J1548.

Similarly, none of the transients discussed have been reported to have unusual radio emission like that from VT J1548. While the radio luminosity of VT J1548 is typical of non-jetted TDEs (Alexander et al. 2020), the SED and late-time detections are atypical. We cannot exclude that most of the aforementioned transients show the same radio light curves as VT J1548: none of these transients have published, late-time, broadband radio follow-up. If the late-time emission is caused by an outflow colliding with a dense, torus-like medium, it is particularly important to obtain late-time radio follow-up of transients where there is evidence for large obscuration.

The closest analog in the literature is the delayed radio emission from the TDE ASASSN-15oi reported by Horesh et al. (2021). ASASSN-15oi rebrightened in the radio  $\sim 1400$  days after its initial flare. This event also rebrightened in the X-ray. The radio light curve evolved at an extremely fast rate, similar to VT J1548, and an inhomogeneous synchrotron model was required to fit the observations. Apart from this unusual radio emission, ASASSN-15oi was a relatively typical TDE, unlike VT J1548 (Holoiien et al. 2016; Jiang et al. 2021a).

We conclude that VT J1548 is a unique transient, largely because of its large extinction, slow evolution, and delayed radio flare. While there is no single transient that definitively comes from the same class as VT J1548, by invoking different

levels of obscuration it is plausible that the family of transients proposed by Trakhtenbrot et al. (2019b) (AT2017bgt, OGLE17aaJ, F01004-2237) and the IR transient SDSS J1657+2345 could form a class of similar objects.

## 7.2. A Qualitative Model for VT J1548

Next, we present a physical model that can explain all the above observations, and later we constrain the event that triggered VT J1548. In Figure 11, we show a very qualitative cartoon model. At the center, we have shown an SMBH with an accretion disk. While we do not have direct evidence for an accretion disk, many of the scenarios we discuss in the rest of this section require a disk. Moreover, emission from an AGN-like disk and its corona could explain some of the observed X-rays. The typical outer radius of an AGN accretion disk is a few light days, or  $\sim 10^{-3}$  pc (Mudd et al. 2018).

The clouds surrounding the accretion disk depict the BLR, which produces the broad H $\alpha$ . Given the width of the observed broad H $\alpha$ , we expect that these clouds are located at a distance  $\sim 5 \times 10^{-3}$  pc. The BLR may have existed before the transient, as long as there was no significant ongoing accretion that would have illuminated the BLR and produced observable broad lines in the archival SDSS spectrum. Alternatively, the BLR could have formed via a dusty wind driven from the accretion disk, as has been proposed in some AGN models (Czerny & Hrynewicz 2011).

Outside of the BLR, we show coronal line-emitting clouds orbiting the SMBH, and a large dusty torus. The torus is not depicted as a standard doughnut, which is an oversimplification of the true structure and fails to predict some observations (e.g., Mason et al. 2006; Ramos Almeida et al. 2009). Instead, we adopt a clumpy, thick, flared, and extended gaseous disk. As discussed by Hopkins et al. (2012) and references therein, galactic-scale inflows trigger a series of gravitational instabilities on small scales, which produce a thick, eccentric disk near

the SMBH without requiring active accretion. The orientation of the disk may be twisted and misaligned with the inner accretion disk, although we depict it as perfectly aligned for simplicity.

The observer is along a line of sight through the edge of the torus such that there is significant extinction, but the line of sight is not completely obscured as in Type 2 AGN. We expect the line of sight to have a column density  $\log N_{\text{H}}/\text{cm}^{-2} \gtrsim 21.5$  given the constraints on the broad Balmer decrement.

We expect the torus to extend outward from at least  $\sim 0.4$  pc given the constraints from the MIR emission (Section 6.1). At 0.4 pc the temperature of the torus is  $\sim 1000$  K, and the dust interior to this radius is hotter. Dust that has been heated to  $T_{\text{sub}} \sim 1600$  K (Lu et al. 2016) is sublimated.

The coronal line-emitting gas is represented by clouds at roughly the same distance ( $\sim 0.8$  pc) as the MIR-emitting gas and outflow. These clouds form from a hot, dusty wind driven by radiation pressure from the edge of the torus (Mullaney & Ward 2008; Gelbord et al. 2009; Dorodnitsyn & Kallman 2012). As the dusty clouds are accelerated off of the torus, the dust sublimates and releases the iron that produces the coronal line emission. While similar clouds are likely driven from the lower side of the torus, these would be highly extincted because they lie on a line of sight through the center of the torus. For simplicity, we do not draw them. While the geometry depicted may not produce the exact coronal line profiles observed, given uncertainties in the torus shape and dusty wind directions and kinematics, we are confident that there is a geometry which could replicate the observations.

Finally, we have drawn an outflow beginning at the accretion disk and that has collided with parts of the torus at a radius  $\sim 0.1$  pc, corresponding to the best-fit radius from our synchrotron model. This radius is roughly consistent with the distance to the MIR-emitting dust. A wide angle outflow is required to explain the multiple synchrotron components (see Alexander et al. 2020, for a discussion of possible origins). We will discuss some of these possibilities in the following sections. While the exact position of this outflow is unknown, we emphasize that it need not be colliding with a uniform medium. Parts of the outflow may be incident on denser parts of the torus, and that could cause the unusual radio SED.

Coronal line emitters are generally interpreted as originating from one of three classes of transients: extreme AGN variability, TDEs, or supernovae. In the following subsections, we discuss each of these possibilities in turn. We expect that our cartoon applies regardless of the exact cause of the flare, unless the flare was triggered by a slightly off-nuclear event (e.g., a supernova). In this case, we are observing the event through some abnormally thick cloud of material. We will discuss this possibility briefly in the following section.

### 7.3. Is VT J1548 a Supernova?

We consider it unlikely that VT J1548 is caused by a supernova because of its luminosity and timescale. The difficulties of interpreting ECLEs as supernovae have been discussed in many previous papers (e.g., Wang et al. 2011, 2012; Frederick et al. 2019), so we only briefly consider it here. Only a few Type IIn supernovae are observed to have coronal line emission. One of the SN IIn with the brightest coronal line emission was SN 2005ip, but by  $\sim 1000$  days the [Fe X] emission was only at  $\sim 10^{37}$  erg s $^{-1}$  (Smith et al. 2009), which is a factor of  $\sim 100$  dimmer than we observe. At no point

during the evolution of SN 2005ip was the [Fe X] emission within a factor of  $\sim 10$  as bright as observed from VT J1548. Of course, VT J1548 may be the most extreme coronal line-emitting supernova seen to date. The X-ray luminosity  $\sim 10^{42-43}$  erg s $^{-1}$  required to produce the coronal lines is unprecedented for supernova—one of the brightest, long-duration X-ray-emitting supernova, SN1988Z, was only detected at  $\sim 10^{41}$  erg s $^{-1}$  (Fabian & Terlevich 1996).

The MIR emission from VT J1548 is difficult to reconcile with a supernova interpretation. Consider the case where the MIR photons are emitted by dust that is ejected by the supernova. The observed MIR emission is consistent with a distance  $\sim 0.4$  pc. To reach this radius within  $\sim 1$  yr, the ejecta must have moved at a velocity  $\sim c$ . This is extraordinarily fast, so instead we invoke preexisting material. The supernova either occurred in the galactic nucleus so that it is obscured by the torus, or the supernova is obscured by a torus-like quantity of dust outside the nucleus. Both of these scenarios are unusual, and combined with the extreme X-ray luminosity required to power the emission, we disfavor the supernova interpretation.

### 7.4. Is VT J1548 a TDE?

Next, we assess whether VT J1548 is consistent with a TDE. ECLEs are often attributed to TDEs (e.g., Wang et al. 2012), although it is difficult to distinguish between AGN accretion variability (see next section) and TDEs. The observed coronal lines would be excited by the soft X-rays and UV continuum produced by the TDE (e.g., Wang et al. 2012). A complication is that many TDEs show bright optical light curves (e.g., van Velzen et al. 2021), which we do not observe from VT J1548. However, an increasing number of optically faint TDEs are being discovered (see Sazonov et al. 2021, for optically faint X-ray selected TDEs). The optical emission from TC0221 may be heavily extincted (see example TDE light curves in Figure 1). The flare may have occurred during a gap in survey coverage. Alternatively, the TDE may have been optically dim. TDEs associated with SMBHs with masses  $\log M_{\text{BH}}/M_{\odot} < 6$  may lack the optically thick gas layer which reprocesses higher energy photons and dominates the optical emission (Lu & Bonnerot 2020).

The timescale of VT J1548 may also pose a problem: standard TDEs are expected to rise on short ( $\sim 10$  s of days) timescales, and they generally fade according to a canonical  $t^{-5/3}$  power law (see Gezari 2021, for a review). Example optical light curves are overplotted in Figure 1. The IR emission from VT J1548 rises over  $\gtrsim 2$  yr. As we discussed in Section 6.1, a prompt, high-energy transient may be able to produce a slowly evolving, MIR flare. Because MIR photons emitted from the far side of the torus have to travel an extra distance  $\sim 2R_{\text{emit}}$  for an emitting radius  $R_{\text{emit}}$ , the flare is smoothed out over a time period  $2R_{\text{emit}}/c$ .

If the observed MIR emission is the echo of a bright, prompt TDE, we have to invoke some delayed X-ray emission to explain our X-ray detections. We might expect dim, late-time X-ray detections from a viscous accretion disk, although whether such disks are expected is uncertain. van Velzen et al. (2019) reported the detection of late-time (5–10 yr post-flare) transient UV emission from eight optical TDE hosts, which is inconsistent with this late-time model, but could be explained as emission from unobscured accretion disks with long viscous timescales. Similarly, Jonker et al. (2020) detected late-time

(5–10 yr post-flare) X-ray emission from TDE candidates. Simulations of TDE evolution may have incorrectly predicted the late-time light-curve evolution, possibly because of incorrect viscosity assumptions. If a slowly evolving viscous disk is present in SDSS J1548, we would expect the MIR flare to fade extremely slowly (i.e., decades timescale).

Late-time interactions between an outflow launched during the initial TDE and a dusty torus are also able to produce delayed X-ray emission at a luminosity  $\sim 10^{41-42}$  erg s $^{-1}$  (Mou et al. 2021). This model can also explain the brightening in the radio via shocks due to the outflow hitting the torus, and predicts that this event should be  $\gamma$ -ray bright (Mou & Wang 2021).

Alternatively, we may be witnessing a TDE that evolves slowly because of delayed accretion disk formation (although see van Velzen et al. 2019; Jonker et al. 2020). TDE accretion disks may form when stellar debris streams collide because of general relativistic precession, eventually dissipating enough energy to collapse (Guillochon & Ramirez-Ruiz 2015). The precession is correlated with the SMBH mass: stellar streams orbiting SMBHs with  $\log M_{\text{BH}}/M_{\odot} \lesssim 6$  may take years for the debris to precess sufficiently to cause collisions (Guillochon & Ramirez-Ruiz 2015). The slow disk formation erases information about the mass fallback rate, which usually sets the light-curve decay time to  $t^{-5/3}$ . TDEs with delayed accretion disks decay following a power law  $\sim t^{-1}$  (Guillochon & Ramirez-Ruiz 2015).

This delayed accretion disk model also requires no preexisting accretion disk. We have invoked a torus to explain the IR emission from VT J1548, but some models predict that tori are only hosted by AGN with sufficiently large luminosities ( $\gtrsim 10^{39}$  erg s $^{-1}$  for a  $\log M_{\text{BH}}/M_{\odot} \sim 6$  SMBH; Höning & Beckert 2007). As discussed by Hopkins et al. (2012), it is feasible that tori can form in quiescent galaxies if dynamical instabilities reminiscent of the bars-within-bars models drive gas to the Galactic center. Regardless, we consider the possibility that SDSS J1548 had a preexisting accretion disk for completeness.

Like TDEs in quiescent galaxies, it is feasible that TDEs in AGN may produce emission years after the initial flare. However, predictions for the observational characteristics of TDEs in AGN are limited. Chan et al. (2020) modeled a TDE in an AGN and predicted light curves that evolve on  $\sim$ month timescales, which is much faster than observed for VT J1548. However, the simulations spanned a very small range of parameter space, so we will have to wait for a more expansive set of models of TDEs in AGN to constrain whether that mechanism could have triggered VT J1548.

In summary, interpreting VT J1548 as a TDE is plausible. In one scenario, the torus geometry and optical depth are such that the long-duration MIR brightening can be produced by a short high-energy flare. Alternatively, TDEs in AGN may simply be able to evolve on very long timescales.

### 7.5. Is VT J1548 an AGN Flare?

VT J1548 may be an extreme AGN event if it is neither a TDE nor a supernova. However, such an event must be unusual. From the low [O III] luminosity  $\sim 10^{39}$  erg s $^{-1}$  and the AGN X-ray/[O III] emission relation from Heckman et al. (2005), we can constrain the historical X-ray luminosity of this source to be  $\ll 10^{42}$  erg s $^{-1}$ . The light travel time through the narrow-line region of an AGN is typically  $10^{2-3}$  yr, so we know

that the X-ray luminosity from this source over that time period must be  $\ll 10^{42}$  erg s $^{-1}$ . Hence, flares such as that observed must occur infrequently.

Variable obscuration can cause bright flares on the orbital timescale of the obscuring cloud (e.g., Stern et al. 2018) but could not explain most all of the other transient emission, such as the broad H $\alpha$ , and we do not consider it further.

Alternatively, VT J1548 may be a CL AGN (also see Miniutti et al. 2019; Arcodia et al. 2021 for examples of more phenomena that can trigger AGN flares). CL AGN comprise a rapidly growing class of AGN which transition from Type 1, with a weak continuum and narrow-line emission, to Type 1.8–2, with broad H $\alpha$  and H $\beta$  alongside a strong continuum, or vice versa. These transitions occur on year-decade timescales, and the AGN can fade and/or rise (e.g., Sheng et al. 2017). They are sometimes associated with MIR (Sheng et al. 2017; Stern et al. 2018; Sheng et al. 2020) and X-ray (Parker et al. 2016) variability and flaring.

If VT J1548 is a CL AGN, it is unprecedented. Unlike most CL AGN, SDSS J1548 showed no strong pre-flare variability or evidence for AGN activity (e.g., see candidates in Yang et al. 2018), although this might be a selection effect since CL AGN candidates are often identified by their pre-flare variability. No unambiguous CL AGN with the unusual radio emission and high Eddington ratio of VT J1548 has been observed to date, although radio follow-up of CL AGN is limited. The CL AGN 013815+00 is notable because it brightens in both the optical and the radio (Hameury 2020). Similarly, Mrk 590 underwent multiple transitions between Seyfert types in the last 30 yr and shows some evidence for radio variability (Koay et al. 2016; Yang et al. 2021). A more complete sample of radio-selected, optical/UV/IR flaring CL AGN, or a comprehensive follow-up program to measure the radio light curves of ongoing CL AGN are key to understanding the expected radio signatures.

Flaring galaxies with  $\log M_{\text{BH}}/M_{\odot} \lesssim 8$  are difficult to unambiguously classify as a TDE or AGN flare, in part because AGN accretion disks still present mysteries: observations of large amplitude variability in AGN are becoming common, and most accretion disk models do not predict frequent, large variability, but instead explain these flares by *instabilities* (Lawrence 2018). Large uncertainties in the relevant timescales and flare amplitudes renders any comparison to observation difficult.

NGC 3599 exemplifies this difficulty. This galaxy underwent a slow, soft X-ray flare that rose over multiple years (Saxton et al. 2015). It lacked observations between the rise and decay, which complicated the interpretation. However, the slow timescale is atypical of normal, prompt TDEs, although, as we have discussed, it is likely that some TDEs can evolve on much longer timescales and cannot be excluded as a trigger of the flare in NGC 3599. Saxton et al. (2015) suggested the Lightman–Eardley disk instability as one possible cause of the flare. The instability arises because Shakura & Sunyaev (1973) thin accretion disks become unstable when radiation pressure dominates over thermal pressure. This condition is fulfilled in the inner regions of any disk that is accreting at a near-Eddington luminosity. The instability manifests as a limit-cycle behavior. When the disk is bright and highly accreting, the inner disk is unstable and empties, which reduces the accretion rate. The inner disk slowly refills, eventually returning to the high accretion state and repeating the cycle. The rise time to the

high accretion rate state is set by the time required to heat the inner disk, which depends strongly on the viscosity prescription but must be greater than (Saxton et al. 2015)

$$R_{\text{trunc}} / c_s \sim 1 \text{ month} \left( \frac{R_{\text{trunc}}}{100 R_g} \right) \left( \frac{M_{\text{BH}}}{10^6 M_\odot} \right), \quad (16)$$

where  $R_{\text{trunc}}$  is the radius at which the disk will become truncated and  $c_s$  is the sound speed.  $R_g$  is the gravitational radius of the SMBH. After the rise, the emission plateaus for an unconstrained time as the inner disk is cleared out. Once the inner disk is empty, the emission will decay to the low state. The decay time is poorly constrained, but it is expected to be faster than the rise time.

Like NGC 3599, VT J1548 evolves on the correct timescales to be explained by the Lightman–Eardley instability. In the future, we can more definitively constrain this possibility by monitoring the evolution of VT J1548 for evidence of (1) a decay time that is much more rapid than the rise time and (2) a repeat flare on a many-decade timescale. Even if such behavior is observed, the interpretation is complicated. The Lightman–Eardley instability cannot be considered in isolation: other instabilities are predicted in the inner disk. For example, the ionization instability applies to cool ( $T \sim 6000$  K) regions of the disk and is the result of the strong temperature and density dependence of the opacity of partially ionized hydrogen (Hameury 2020).

Moreover, it is unclear whether the Lightman–Eardley instability actually occurs in low-mass accreting BHs, let alone AGN (Janiuk & Czerny 2011). The Shakura & Sunyaev (1973) viscosity is an oversimplification, and there is some evidence that a more physical viscosity prescription eliminates the instability (Blaes et al. 2006). Similarly, while the ionization instability is well established for dwarf novae (see Hameury 2020, for a review), it has not been definitively observed in AGN.

In summary, VT J1548 may be a CL AGN, although its lack of strong AGN signatures and bright radio flare are unusual. Observations of a repeat flare or a fast decay time could support a CL AGN origin.

### 7.6. Future Work and Observations

It is extremely difficult to unambiguously determine the cause of VT J1548, as is a common issue for like transients. In many cases, extreme AGN variability is as feasible an explanation as a TDE-like transient. In this section, we suggest future observations and theoretical work that could help constrain the origin of VT J1548 and like events. We begin with possible observations.

1. *Early time spectroscopic follow-up of VT J1548-like transients.* While inapplicable to VT J1548 itself, this follow-up could help constrain the presence of features such as He II and Bowen fluorescence lines that may have faded by the late-time observations of VT J1548.
2. *Long-term NIR/MIR monitoring of VT J1548 (and similar transients).* Knowledge of the IR evolution is essential to constrain the origin of the flare. If this event is triggered by a TDE, we expect the emission to begin fading soon. If VT J1548 is an AGN flare, it could remain bright for decades or longer. Combined with theoretical modeling of AGN flares and TDE in AGN, the fade time of the

event may constrain its origin. Some AGN flares may fade more quickly than a typical TDE (Saxton et al. 2015). We are actively monitoring VT J1548 in the NIR. If SDSS J1548 is also monitored in the MIR for multiple decades, we could also constrain the presence of a repeat flare, which may provide a smoking gun for extreme AGN variability.

3. *Long-term optical spectroscopic monitoring.* We are actively following up VT J1548 with optical spectrographs to determine the evolution of the broad Balmer emission, the coronal lines (both profile and flux), as well as any other features that may begin to evolve.
4. *Long-term X-ray/radio (100s of MHz–GHz) monitoring.* Long-term X-ray/radio monitoring will allow us to constrain the origin of emission at both wavelengths. As we have mentioned the importance of this follow-up throughout the text, we do not discuss it further.
5. *Optical IFU follow-up.* Optical IFU observations would allow us to constrain whether the preexisting high-ionization emission, such as the [O III] lines, are nuclear or very extended. Then, we could constrain the history of AGN activity.

This list is far from exhaustive (e.g., polarimetric observations and hard X-ray spectra would prove useful).

On the theoretical side, the most critical work is extensive simulations of TDEs in AGN-like environments. In particular, given the difficulty of getting early time follow-up of these events, detailed simulations of the fading of the TDE emission would be valuable. It would also be useful to model the response of an AGN torus to a TDE-like flare accounting for different torus models, inclination angles, and flare durations/shapes. Finally, detailed models of the expected evolution of coronal line flux and profile during a TDE-like event would prove extremely valuable toward constraining the timescales of ECLEs, and hence their triggers.

## 8. Conclusions

We have presented the first radio-selected ECLE, VT J1548, and its host, SDSS J1548. This work can be summarized as follows:

1. VT J1548 is associated with a MIR flare that rose in  $\sim 900$  days and has plateaued with a constant color corresponding to a blackbody with  $T \sim 1000$  K and  $L \sim 0.1 L_{\text{edd}}$ . (Figure 1). Radio emission turned on during the WISE flare. The radio SED can be modeled as synchrotron from an outflow incident on an inhomogeneous medium. No optical flare is detected. Transient, X-ray emission with  $L_{0.2-10 \text{ keV}} \sim 10^{42}$  erg s $^{-1}$  was detected  $\sim 1000$  days after the MIR flare began.
2. Transient coronal lines with  $L_{\text{cor}} \sim L_{[\text{O III}]}$  and broad H $\alpha$  emission are detected  $\sim 1000$  days post-flare. The coronal line emission from VT J1548 is double peaked with a velocity separation  $\sim 230$  km s $^{-1}$  (Figure 5). The broad H $\alpha$  emission has FWHM  $\sim 1900$  km s $^{-1}$ . No broad H $\beta$  is detected, suggesting a high extinction  $E(B - V) \gtrsim 0.7$  (Figure 6).
3. SDSS J1548, the host of VT J1548, is an S0 galaxy at  $z = 0.031$  ( $d_L = 137$  Mpc). Its pre-flare line ratios are consistent with no or weak AGN activity (Figure 4). Its pre-flare WISE color was inconsistent with typical AGN colors

- and it showed no significant MIR variability. It hosts a low-mass SMBH with  $\log M_{\text{BH}}/M_{\odot} = 6.48 \pm 0.33$ .
4. VT J1548 is unique when compared to other transients, although it shares individual properties with other objects (Table 6). It is reminiscent of the class reported by Trakhtenbrot et al. (2019b) and the MIR flare SDSS J1657+2345 (Yang et al. 2019), which are all slowly evolving. None of these events emit in the radio like VT J1548, nor do they show coronal line emission. The only transient with radio emission that resembles that from VT J1548 is the TDE candidate ASASSN-15oi, which was detected at late times in the X-ray and radio with an unusual radio SED, although none of its other properties resemble VT J1548.
  5. VT J1548 can be modeled with a BLR ( $\sim 10^{-3}$  pc) surrounded by a dusty torus (Figure 11). At the inner edge of the torus ( $\sim 0.4$  pc), sublimated dust accelerated in a radiation-driven wind causes the formation of coronal line-emitting clouds. Alternatively, the coronal line-emitting clouds are orbiting the SMBH. Some of the dust in the torus is heated to produce the MIR flare. The synchrotron-emitting outflow is launched near the SMBH and collides with the torus.
  6. VT J1548 could plausibly have been triggered by a TDE or an AGN disk instability. In the TDE scenario, the high observed Eddington ratio, the radio emission, and the slow evolution are unusual. In the AGN scenario, the lack of strong pre-flare AGN activity is uncommon, the high Eddington ratio is unexpected, and the unusual radio emission is unprecedented.

We have emphasized the difficulty of distinguishing between an AGN flare and a TDE in a highly obscured galaxy with evidence for weak AGN activity. Such efforts are particularly complicated because of the freedom in structure and optical depth of a torus, which can eliminate most all timescale information if the inner  $\sim$ parsec of the galaxy is too extincted to be directly visible. Moreover, the uncertainty in the timescale, luminosity, and multiwavelength properties of flares from TDEs (in both AGN and quiescent galaxies) as well as AGN disk instability-driven flares renders it difficult to distinguish between these events even with early time follow-up. While it may be difficult to constrain the origins of individual events, population studies are key to characterizing the range and relative frequency of these different flares. The identification of *classes* of transients is likely to be less ambiguous if members are observed from a range of inclination angles over a variety of time baselines in multiple wave bands.

We would like to thank Sterl Phinney for useful discussions. We would like to thank Phil Hopkins for insight into the formation and evolution of AGN tori. Finally, we would like to thank the entire ZTF TDE/AGN group for useful discussions, and in particular, Suvi Gezari and Sjoert van Velzen.

C.J.L. acknowledges support from the National Science Foundation under grant No. 2022546.

This work made use of data supplied by the UK Swift Science Data Centre at the University of Leicester. The National Radio Astronomy Observatory is a facility of the National Science Foundation operated under cooperative agreement by Associated Universities, Inc. CIRADA is funded by a grant from the Canada Foundation for Innovation 2017 Innovation Fund (Project 35999), as well as by the Provinces of

Ontario, British Columbia, Alberta, Manitoba and Quebec. Some of the data presented herein were obtained at the W. M. Keck Observatory, which is operated as a scientific partnership among the California Institute of Technology, the University of California and the National Aeronautics and Space Administration. The Observatory was made possible by the generous financial support of the W. M. Keck Foundation. The authors wish to recognize and acknowledge the very significant cultural role and reverence that the summit of Maunakea has always had within the indigenous Hawaiian community. We are most fortunate to have the opportunity to conduct observations from this mountain. Funding for the SDSS and SDSS-II has been provided by the Alfred P. Sloan Foundation, the Participating Institutions, the National Science Foundation, the U.S. Department of Energy, the National Aeronautics and Space Administration, the Japanese Monbukagakusho, the Max Planck Society, and the Higher Education Funding Council for England. The SDSS website is <http://www.sdss.org/>. The SDSS is managed by the Astrophysical Research Consortium for the Participating Institutions. The Participating Institutions are the American Museum of Natural History, Astrophysical Institute Potsdam, University of Basel, University of Cambridge, Case Western Reserve University, University of Chicago, Drexel University, Fermilab, the Institute for Advanced Study, the Japan Participation Group, Johns Hopkins University, the Joint Institute for Nuclear Astrophysics, the Kavli Institute for Particle Astrophysics and Cosmology, the Korean Scientist Group, the Chinese Academy of Sciences (LAMOST), Los Alamos National Laboratory, the Max-Planck-Institute for Astronomy (MPIA), the Max-Planck-Institute for Astrophysics (MPA), New Mexico State University, Ohio State University, University of Pittsburgh, University of Portsmouth, Princeton University, the United States Naval Observatory, and the University of Washington. Based on observations obtained with the Samuel Oschin 48 inch Telescope at the Palomar Observatory as part of the Zwicky Transient Facility project. ZTF is supported by the National Science Foundation under grant No. AST-1440341 and a collaboration including Caltech, IPAC, the Weizmann Institute for Science, the Oskar Klein Center at Stockholm University, the University of Maryland, the University of Washington, Deutsches Elektronen-Synchrotron and Humboldt University, Los Alamos National Laboratories, the TANGO Consortium of Taiwan, the University of Wisconsin at Milwaukee, and Lawrence Berkeley National Laboratories. Operations are conducted by COO, IPAC, and UW.

*Facility:* Swift(XRT), Keck I(LRIS), Keck II(ESI), VLA, WISE, XMM-Newton(EPIIC).

*Software:* Astropy (Robitaille et al. 2013; Astropy Collaboration et al. 2018), Matplotlib (Hunter 2007), NumPy (Harris et al. 2020; van der Walt et al. 2011), Pandas (pandas development team 2020; McKinney 2010), SciPy (Virtanen et al. 2020), dynesty (Speagle 2020; Skilling 2004; Higson et al. 2019), emcee (Foreman-Mackey et al. 2013), pybdsf (Mohan & Rafferty 2015).

## Appendix A VLASS Transient Search

We identified transient sources between the VLASS Epoch 2.1 and Epoch 1 observations using the following procedure. First, we ran the source extractor PyBDSF (Mohan & Rafferty 2015) on the VLASS Epoch 2.1 quicklook images

provided by the National Radio Astronomy Observatory (NRAO; Lacy et al. 2020), spanning  $\sim 17,000$  deg $^2$ . We identify point-source candidates as regions within the Epoch 2.1 images where contiguous *islands* of  $>4\sigma$  pixels surrounding a peak pixel of  $>6\sigma$  can be well described by a single 2D Gaussian. Some of these candidates are due to deconvolution artifacts: typically sidelobes near bright sources or extended stripes. We flag the majority of these artifacts in an automated way using a stripe detection algorithm and by comparing the pixels near the source to the pixels in the 1' region around it (D. Dong et al. 2022, in preparation). After flagging likely artifacts, we estimate the flux of each point-source candidate as its peak pixel value, and the uncertainty as the local value in the quicklook RMS maps provided by the NRAO. We then check the corresponding location in the Epoch 1.1 image data. Based on the local pixel values in each epoch, we estimate the probability of variability by comparison with a grid of Monte Carlo simulations of sources embedded in Gaussian noise (D. Dong et al. 2022, in preparation). We create an initial transient catalog in which we retain sources that have (1) no artifact flags, (2) a  $>90\%$  probability of being variable, (3) a peak  $>7\sigma$  in Epoch 2.1, and (4) a peak  $<3\sigma$  in Epoch 1.1. We visually inspected all transient candidates in the initial catalog, removing the artifacts that were missed by our automated filters. The remaining sources comprise our final transient catalog.

## Appendix B Spectral Fitting Methods

We use a consistent method to fit the optical emission lines in all of our observations. First, we correct the spectrum for Milky Way extinction using  $A_V = 0.1606$  and  $R_V = 3.1$  (Schlafly & Finkbeiner 2011; Fitzpatrick 1999). We remove the stellar continuum using a full spectrum fit with the penalized pixel-fitting (pPXF) method. We use the implementation of pPXF from Cappellari & Emsellem (2004), Cappellari (2017) with the default MILES templates (Vazdekis et al. 2010). We run the fit using recommended procedures to determine the appropriate regularization error and refer the reader to the pPXF documentation for details. Rather than mask the emission lines during this fit, we include Gaussian components for each emission line, and allow the parameters for narrow forbidden, narrow allowed, and broad lines to float separately. These Gaussian fits are not used to measure the line fluxes; we only include emission line components to prevent the lines from biasing the pPXF fit. Our exact treatment of the emission lines does not affect our results. We also include a multiplicative normalization component that is a degree 10 polynomial.

The MILES templates cover the wavelength range 3525–7500 Å, which does not span the full wavelength range of our observations. Hence, we perform an additional median subtraction to normalize the remaining parts of the spectrum, as well as to correct for any continuum flux that was poorly removed by the pPXF fit. First, we subtract the best-fit stellar continuum and emission lines found by pPXF from our observed spectrum. We subtract the value of the best-fit stellar continuum at the nearest available pixel from the portions of the spectrum not covered by the template fit. From this procedure, we have a preliminary continuum-subtracted spectrum. Next, we median smooth this preliminary continuum-subtracted spectrum with a

kernel of  $\sim 130$  pixels, which we found was sufficient for both the LRIS and SDSS spectra. We identify all points in the spectrum that are  $>10\sigma$  from the resulting median smoothed continuum and mask them, as well as the  $\sim 10$  pixels neighboring those points. Then, we median smooth the preliminary continuum-subtracted spectrum a second time with these pixels masked. This gives us a correction to the continuum, which we subtract from our preliminary continuum-subtracted spectrum to obtain the final continuum-subtracted spectrum.

Next, we measure the emission line fluxes from the final continuum-subtracted spectrum. We model each line with as many Gaussian profiles are required, and we specify throughout the text any case where multiple components are needed. We let the width of the Gaussians float independently for different lines, and include a broad component if necessary. We also include a linear continuum component to account for any residual flux. We fit each emission line separately unless multiple emission lines are so close that they cannot be fit independently (e.g., the H $\alpha$  and [N II] lines). We fit a region around each line that includes a  $\sim 10$ –20 Å continuum region.

We run the emission line fit using the *dynesty* Nested Sampler (Speagle 2020; Skilling 2004). Our stopping condition is  $\Delta \log \mathcal{Z} = 5$ , which we verify does not affect our results. Unless otherwise specified, we report  $1\sigma$  errors on all line fluxes.

## Appendix C Measurement of the Bulge Velocity Dispersion

We measure the bulge velocity dispersion using the  $R \sim 13,000$  ESI spectrum of SDSS J1548 following the methodology in Wevers et al. 2017. To ensure that we are measuring the *bulge* velocity dispersion, we consider two different methods of extracting the host spectrum: first, we use the spectrum extracted from the full slit; second, we isolate the bulge by using the spectrum extracted from a region centered on the peak galaxy light and with width 0''.5, which roughly corresponds to the seeing during the observation. We find no significant difference in the results.

We use the Cappellari (2017) implementation of pPXF to measure the velocity dispersion. First, we mask all emission lines in the spectrum, including the hydrogen Balmer lines and all TDE features. We fit the spectrum using the Prugniel et al. (2007) and Prugniel & Soubiran (2001) high-resolution ( $R \sim 10,000$ ) template library. We run the fit using the recommended pPXF settings. The best-fit velocity dispersion is  $\sim 66$  km s $^{-1}$ . Removing the intrinsic resolution ( $\sim 22$  km s $^{-1}$ ) only changes the result by a few kilometers per second. Next, we convert to SMBH mass using the relation from Ferrarese & Ford (2005). The intrinsic scatter in the  $M_{\text{BH}} - \sigma_*$  relation strongly dominates our results, although we also propagate through both the uncertainties in the velocity dispersion measurement and assumed uncertainties in the intrinsic resolution. We find an SMBH mass  $\log M_{\text{BH}}/M_{\odot} = 5.98 \pm 0.38$ . Alternatively, the more recent  $M_{\text{BH}} - \sigma_*$  relation from Kormendy & Ho (2013) gives  $\log M_{\text{BH}}/M_{\odot} = 6.48 \pm 0.33$ , which is consistent with that of Ferrarese & Ford (2005) within  $1\sigma$ . We adopt the latter calibration because it includes more low-mass galaxies.

## ORCID iDs

Jean J. Somalwar  <https://orcid.org/0000-0001-8426-5732>  
 Vikram Ravi  <https://orcid.org/0000-0002-7252-5485>

Dillon Dong [ID](https://orcid.org/0000-0001-9584-2531) <https://orcid.org/0000-0001-9584-2531>  
 Matthew Graham [ID](https://orcid.org/0000-0002-3168-0139) <https://orcid.org/0000-0002-3168-0139>  
 Gregg Hallinan [ID](https://orcid.org/0000-0002-7083-4049) <https://orcid.org/0000-0002-7083-4049>  
 Casey Law [ID](https://orcid.org/0000-0002-4119-9963) <https://orcid.org/0000-0002-4119-9963>  
 Wenbin Lu [ID](https://orcid.org/0000-0002-1568-7461) <https://orcid.org/0000-0002-1568-7461>

## References

- Ahumada, R., Prieto, C. A., Almeida, A., et al. 2020, *ApJS*, **249**, 3  
 Alexander, K. D., van Velzen, S., Horesh, A., & Zauderer, B. A. 2020, *SSRv*, **216**, 81  
 Arcodia, R., Merloni, A., Nandra, K., et al. 2021, *Natur*, **592**, 704  
 Assef, R. J., Stern, D., Noiro, G., et al. 2018, *ApJS*, **234**, 23  
 Astropy Collaboration, Price-Whelan, A. M., SipHocz, B. M., et al. 2018, *AJ*, **156**, 123  
 Auchettl, K., Guillochon, J., & Ramirez-Ruiz, E. 2017, *ApJ*, **838**, 149  
 Bade, N., Komossa, S., & Dahlem, M. 1996, *A&A*, **309**, L35  
 Baldwin, J. A., Phillips, M. M., & Terlevich, R. 1981, *PASP*, **93**, 5  
 Bellm, E. C., Kulkarni, S. R., Barlow, T., et al. 2019, *PASP*, **131**, 068003  
 Björnsson, C. I. 2013, *ApJ*, **769**, 65  
 Björnsson, C. I., & Keshavarzi, S. T. 2017, *ApJ*, **841**, 12  
 Blaes, O. M., Davis, S. W., Hirose, S., Krolik, J. H., & Stone, J. M. 2006, *ApJ*, **645**, 1402  
 Blanchard, P. K., Nicholl, M., Berger, E., et al. 2017, *ApJ*, **843**, 106  
 Boller, T., Freyberg, M. J., Truemper, J., et al. 2016, *A&A*, **588**, A103  
 Brown, J. S., Holoiien, T. W. S., Auchettl, K., et al. 2017, *MNRAS*, **466**, 4904  
 Burrows, D. N., Hill, J. E., Nosek, J. A., et al. 2005, *SSRv*, **120**, 165  
 Calzetti, D., Armus, L., Bohlin, R. C., et al. 2000, *ApJ*, **533**, 682  
 Cappellari, M. 2017, *MNRAS*, **466**, 798  
 Cappellari, M., & Emsellem, E. 2004, *PASP*, **116**, 138  
 Cash, W. 1979, *ApJ*, **228**, 939  
 Chabrier, G. 2003, *PASP*, **115**, 763  
 Chambers, K. C., Magnier, E. A., Metcalfe, N., et al. 2016, arXiv:1612.05560  
 Chan, C.-H., Piran, T., & Krolik, J. H. 2020, *ApJ*, **903**, 17  
 Chandra, P., Nayana, A. J., Björnsson, C. I., et al. 2019, *ApJ*, **877**, 79  
 Chevalier, R. A. 1998, *ApJ*, **499**, 810  
 Cid Fernandes, R., Stasińska, G., Mateus, A., & Vale Asari, N. 2011, *MNRAS*, **413**, 1687  
 Condon, J. J., Cotton, W. D., Greisen, E. W., et al. 1998, *AJ*, **115**, 1693  
 Conroy, C., & Gunn, J. E. 2010, *ApJ*, **712**, 833  
 Conroy, C., Gunn, J. E., & White, M. 2009, *ApJ*, **699**, 486  
 Czerny, B., & Hrynewicz, K. 2011, *A&A*, **525**, L8  
 Del Zanna, G., Dere, K. P., Young, P. R., & Landi, E. 2021, *ApJ*, **909**, 38  
 Dere, K. P., Landi, E., Mason, H. E., Monsignori Fossi, B. C., & Young, P. R. 1997, *A&AS*, **125**, 149  
 Dey, A., Schlegel, D. J., Lang, D., et al. 2019, *ApJ*, **157**, 168  
 Dong, X., Wang, T., Wang, J., et al. 2008, *MNRAS*, **383**, 581  
 Donley, J. L., Brandt, W. N., Eracleous, M., & Boller, T. 2002, *AJ*, **124**, 1308  
 Dorodnitsyn, A., & Kallman, T. 2012, *ApJ*, **761**, 70  
 Dou, L., Wang, T.-g., Jiang, N., et al. 2016, *ApJ*, **832**, 188  
 Dou, L., Wang, T., Yan, L., et al. 2017, *ApJL*, **841**, L8  
 Draine, B. T. 2011a, Physics of the Interstellar and Intergalactic Medium (Princeton, NJ: Princeton Univ. Press)  
 Draine, B. T. 2011b, *ApJ*, **732**, 100  
 Draine, B. T., & Lee, H. M. 1984, *ApJ*, **285**, 89  
 Esquej, P., Saxton, R. D., Freyberg, M. J., et al. 2007, *A&A*, **462**, L49  
 Evans, P. A., Beardmore, A. P., Page, K. L., et al. 2007, *A&A*, **469**, 379  
 Fabian, A. C., & Terlevich, R. 1996, *MNRAS*, **280**, L5  
 Ferrarese, L., & Ford, H. 2005, *SSRv*, **116**, 523  
 Fitzpatrick, E. L. 1999, *PASP*, **111**, 63  
 Flewelling, H. A., Magnier, E. A., Chambers, K. C., et al. 2020, *ApJS*, **251**, 7  
 Foreman-Mackey, D., Hogg, D. W., Lang, D., & Goodman, J. 2013, *PASP*, **125**, 306  
 Frank, J., & Rees, M. J. 1976, *MNRAS*, **176**, 633  
 Frederick, S., Gezari, S., Graham, M. J., et al. 2019, *ApJ*, **883**, 31  
 Frederick, S., Gezari, S., Graham, M. J., et al. 2021, *ApJ*, **920**, 56  
 Gelbord, J. M., Mullaney, J. R., & Ward, M. J. 2009, *MNRAS*, **397**, 172  
 Gezari, S. 2021, *ARA&A*, **59**, 33  
 Giannios, D., & Metzger, B. D. 2011, *MNRAS*, **416**, 2102  
 Giommi, P., Angelini, L., Jacobs, P., & Tagliaferri, G. 1992, in ASP Conf. Ser. 25, Astronomical Data Analysis Software and Systems I, ed. D. M. Worrall, C. Biemesderfer, & J. Barnes (San Francisco, CA: ASP), 100  
 Graham, M. J., Kulkarni, S. R., Bellm, E. C., et al. 2019, *PASP*, **131**, 078001  
 Granot, J., & Sari, R. 2002, *ApJ*, **568**, 820  
 Greene, J. E., & Ho, L. C. 2005, *ApJ*, **630**, 122  
 Greene, J. E., Strader, J., & Ho, L. C. 2020, *ARA&A*, **58**, 257  
 Gromadzki, M., Hamanowicz, A., Wyrzykowski, L., et al. 2019, *A&A*, **622**, L2  
 Guillochon, J., & Ramirez-Ruiz, E. 2015, *ApJ*, **809**, 166  
 Gültekin, K., King, A. L., Cackett, E. M., et al. 2019, *ApJ*, **871**, 80  
 Hameury, J. M. 2020, *AdSpR*, **66**, 1004  
 Harris, C. R., Millman, K. J., van der Walt, S. J., et al. 2020, *Natur*, **585**, 357  
 Heckman, T. M., Ptak, A., Hornschemeier, A., & Kauffmann, G. 2005, *ApJ*, **634**, 161  
 Helfand, D. J., White, R. L., & Becker, R. H. 2015, *ApJ*, **801**, 26  
 Hernández-García, L., Masegosa, J., González-Martín, O., et al. 2017, *A&A*, **602**, A65  
 Higson, E., Handley, W., Hobson, M., & Lasenby, A. 2019, *S&C*, **29**, 891  
 Hinkle, J. T., Holoiien, T. W. S., Shappee, B. J., et al. 2021, arXiv:2108.03245  
 Ho, A. Y. Q., Phinney, E. S., Ravi, V., et al. 2019, *ApJ*, **871**, 73  
 Holoiien, T. W. S., Kochanek, C. S., Prieto, J. L., et al. 2016, *MNRAS*, **463**, 3813  
 Höning, S. F., & Beckert, T. 2007, *MNRAS*, **380**, 1172  
 Hopkins, P. F., Hayward, C. C., Narayanan, D., & Hernquist, L. 2012, *MNRAS*, **420**, 320  
 Horesh, A., Cenko, S. B., & Arcavi, I. 2021, *NatAs*, **5**, 491  
 Huertas-Company, M., Aguerri, J. A. L., Bernardi, M., Mei, S., & Sánchez Almeida, J. 2011, *A&A*, **525**, A157  
 Hunter, J. D. 2007, *CSE*, **9**, 90  
 Ilić, D., Popović, L. Č., La Mura, G., Ciroi, S., & Rafanelli, P. 2012, *A&A*, **543**, A142  
 Janiuk, A., & Czerny, B. 2011, *MNRAS*, **414**, 2186  
 Jiang, N., Wang, T., Dou, L., et al. 2021b, *ApJS*, **252**, 32  
 Jiang, N., Wang, T., Hu, X., et al. 2021a, *ApJ*, **911**, 31  
 Jiang, N., Wang, T., Mou, G., et al. 2019, *ApJ*, **871**, 15  
 Jiang, N., Wang, T., Yan, L., et al. 2017, *ApJ*, **850**, 63  
 Johnson, B. D., Leja, J., Conroy, C., & Speagle, J. S. 2021, *ApJS*, **254**, 22  
 Jonker, P. G., Stone, N. C., Generozov, A., van Velzen, S., & Metzger, B. 2020, *ApJ*, **889**, 166  
 Kankare, E., Kotak, R., Mattila, S., et al. 2017, *NatAs*, **1**, 865  
 Kewley, L. J., Groves, B., Kauffmann, G., & Heckman, T. 2006, *MNRAS*, **372**, 961  
 Koay, J. Y., Vestergaard, M., Bignall, H. E., Reynolds, C., & Peterson, B. M. 2016, *MNRAS*, **460**, 304  
 Komossa, S., & Bade, N. 1999, *A&A*, **343**, 775  
 Komossa, S., Zhou, H., Wang, T., et al. 2008, *ApJL*, **678**, L13  
 Kool, E. C., Reynolds, T. M., Mattila, S., et al. 2020, *MNRAS*, **498**, 2167  
 Korista, K. T., & Ferland, G. J. 1989, *ApJ*, **343**, 678  
 Kormendy, J., & Ho, L. C. 2013, *ARA&A*, **51**, 511  
 Krolik, J., Piran, T., Svirski, G., & Cheng, R. M. 2016, *ApJ*, **827**, 127  
 Kunert-Bajraszewska, M., Wołowska, A., Mooley, K., Kharb, P., & Hallinan, G. 2020, *ApJ*, **897**, 128  
 Lacy, M., Baum, S. A., Chandler, C. J., et al. 2020, *PASP*, **132**, 035001  
 Lawrence, A. 2018, *NatAs*, **2**, 102  
 Leloudas, G., Fraser, M., Stone, N. C., et al. 2016, *NatAs*, **1**, 0002  
 Lu, W., & Bonnerot, C. 2020, *MNRAS*, **492**, 686  
 Lu, W., Kumar, P., & Evans, N. J. 2016, *MNRAS*, **458**, 575  
 Mainzer, A., Bauer, J., Grav, T., et al. 2011, *ApJ*, **731**, 53  
 Malyali, A., Rau, A., Merloni, A., et al. 2021, *A&A*, **647**, A9  
 Margutti, R., Metzger, B. D., Chornock, R., et al. 2017, *ApJ*, **836**, 25  
 Martin, D. C., Fanson, J., Schiminovich, D., et al. 2005, *ApJL*, **619**, L1  
 Masci, F. J., Laher, R. R., Rusholme, B., et al. 2019, *PASP*, **131**, 018003  
 Mason, R. E., Geballe, T. R., Packham, C., et al. 2006, *ApJ*, **640**, 612  
 Mazzalay, X., Rodríguez-Ardila, A., & Komossa, S. 2010, *MNRAS*, **405**, 1315  
 McKinney, W. 2010, in Proc. of the 9th Python in Science Conf., ed. S. van der Walt & J. Millman, 61  
 Mendel, J. T., Simard, L., Palmer, M., Ellison, S. L., & Patton, D. R. 2014, *ApJS*, **210**, 3  
 Metzger, B. D., Giannios, D., & Mimica, P. 2012, *MNRAS*, **420**, 3528  
 Million, C., Fleming, S. W., Shiao, B., et al. 2016, *ApJ*, **833**, 292  
 Miniutti, G., Saxton, R. D., Giustini, M., et al. 2019, *Natur*, **573**, 381  
 Mockler, B., Guillochon, J., & Ramirez-Ruiz, E. 2019, *ApJ*, **872**, 151  
 Mohan, N., & Rafferty, D. 2015, PyBDSF: Python Blob Detection and Source Finder, Astrophysics Source Code Library, ascl:1502.007  
 Mou, G., Dou, L., Jiang, N., et al. 2021, *ApJ*, **908**, 197  
 Mou, G., & Wang, W. 2021, *MNRAS*, **507**, 1684  
 Mudd, D., Martini, P., Zu, Y., et al. 2018, *ApJ*, **862**, 123  
 Mullaney, J. R., & Ward, M. J. 2008, *MNRAS*, **385**, 53  
 Mullaney, J. R., Ward, M. J., Done, C., Ferland, G. J., & Schurch, N. 2009, *MNRAS*, **394**, L16

- Murayama, T., & Taniguchi, Y. 1998, *ApJL*, **503**, L115
- Netzer, H. 2015, *ARA&A*, **53**, 365
- Neustadt, J. M. M., Hololen, T. W. S., Kochanek, C. S., et al. 2020, *MNRAS*, **494**, 2538
- Oke, J. B., Cohen, J. G., Carr, M., et al. 1995, *PASP*, **107**, 375
- Pacholczyk, A. G. 1970, Radio Astrophysics: Nonthermal Processes in Galactic and Extragalactic Sources (San Francisco, CA: Freeman)
- Palaversa, L., Gezari, S., Sesar, B., et al. 2016, *ApJ*, **819**, 151
- pandas development team, T. 2020, pandas-dev/pandas: Pandas, v1.4.2, Zenodo, doi:[10.5281/zenodo.3509134](https://doi.org/10.5281/zenodo.3509134)
- Parker, M. L., Komossa, S., Kollatschny, W., et al. 2016, *MNRAS*, **461**, 1927
- Penston, M. V., Fosbury, R. A. E., Boksenberg, A., Ward, M. J., & Wilson, A. S. 1984, *MNRAS*, **208**, 347
- Perley, D. A. 2019, *PASP*, **131**, 084503
- Piran, T., Svirski, G., Krolik, J., Cheng, R. M., & Shiokawa, H. 2015, *ApJ*, **806**, 164
- Prugniel, P., & Soubiran, C. 2001, *A&A*, **369**, 1048
- Prugniel, P., Soubiran, C., Koleva, M., & Le Borgne, D. 2007, arXiv:[astro-ph/0703658](https://arxiv.org/abs/astro-ph/0703658)
- Ramos Almeida, C., Levenson, N. A., Rodríguez Espinosa, J. M., et al. 2009, *ApJ*, **702**, 1127
- Rees, M. J. 1988, *Natur*, **333**, 523
- Ricci, C., Trakhtenbrot, B., Koss, M. J., et al. 2017, *Natur*, **549**, 488
- Riffel, R., Rodríguez-Ardila, A., & Pastoriza, M. G. 2006, *A&A*, **457**, 61
- Robitaille, T. P., Tollerud, E. J., Greenfield, P., et al. 2013, *A&A*, **558**, A33
- Saulder, C., van Kampen, E., Chilingarian, I. V., Mieske, S., & Zeilinger, W. W. 2016, *A&A*, **596**, A14
- Saxton, R. D., Motta, S. E., Komossa, S., & Read, A. M. 2015, *MNRAS*, **454**, 2798
- Saxton, R. D., Read, A. M., Komossa, S., et al. 2019, *A&A*, **630**, A98
- Sazonov, S., Gilfanov, M., Medvedev, P., et al. 2021, *MNRAS*, **508**, 3820
- Schlafly, E. F., & Finkbeiner, D. P. 2011, *ApJ*, **737**, 103
- Schnorr-Müller, A., Davies, R. I., Korista, K. T., et al. 2016, *MNRAS*, **462**, 3570
- Seyfert, C. K. 1943, *ApJ*, **97**, 28
- Shakura, N. I., & Sunyaev, R. A. 1973, *A&A*, **500**, 33
- Sheinis, A. I., Bolte, M., Epps, H. W., et al. 2002, *PASP*, **114**, 851
- Sheng, Z., Wang, T., Jiang, N., et al. 2017, *ApJL*, **846**, L7
- Sheng, Z., Wang, T., Jiang, N., et al. 2020, *ApJ*, **889**, 46
- Simard, L., Mendel, J. T., Patton, D. R., Ellison, S. L., & McConnachie, A. W. 2011, *ApJS*, **196**, 11
- Skilling, J. 2004, in AIP Conf. Ser. 735, Bayesian Inference and Maximum Entropy Methods in Science and Engineering: 24th Int. Workshop on Bayesian Inference and Maximum Entropy Methods in Science and Engineering, ed. R. Fischer, R. Preuss, & U. V. Toussaint (Melville, NY: AIP), **395**
- Smith, N., Silverman, J. M., Chornock, R., et al. 2009, *ApJ*, **695**, 1334
- Snellen, I. A. G., Schilizzi, R. T., Miley, G. K., et al. 1999, *NewAR*, **43**, 675
- Speagle, J. S. 2020, *MNRAS*, **493**, 3132
- Stern, D., McKernan, B., Graham, M. J., et al. 2018, *ApJ*, **864**, 27
- Strauss, M. A., Weinberg, D. H., Lupton, R. H., et al. 2002, *AJ*, **124**, 1810
- Tadhunter, C., Spence, R., Rose, M., Mullaney, J., & Crowther, P. 2017, *NatAs*, **1**, 0061
- Trakhtenbrot, B., Arcavi, I., MacLeod, C. L., et al. 2019a, *ApJ*, **883**, 94
- Trakhtenbrot, B., Arcavi, I., Ricci, C., et al. 2019b, *NatAs*, **3**, 242
- van der Walt, S., Colbert, S. C., & Varoquaux, G. 2011, *CSE*, **13**, 22
- van Velzen, S., Farrar, G. R., Gezari, S., et al. 2011, *ApJ*, **741**, 73
- van Velzen, S., Gezari, S., Hammerstein, E., et al. 2021, *ApJ*, **908**, 4
- van Velzen, S., Mendez, A. J., Krolik, J. H., & Gorjian, V. 2016, *ApJ*, **829**, 19
- van Velzen, S., Stone, N. C., Metzger, B. D., et al. 2019, *ApJ*, **878**, 82
- Vazdekis, A., Sánchez-Blázquez, P., Falcón-Barroso, J., et al. 2010, *MNRAS*, **404**, 1639
- Viegas-Aldrovandi, S. M., & Contini, M. 1989, *A&A*, **215**, 253
- Virtanen, P., Gommers, R., Oliphant, T. E., et al. 2020, *NatMe*, **17**, 261
- Voges, W. 1993, *AdSpR*, **13**, 391
- Wang, T.-G., Zhou, H.-Y., Komossa, S., et al. 2012, *ApJ*, **749**, 115
- Wang, T.-G., Zhou, H.-Y., Wang, L.-F., Lu, H.-L., & Xu, D. 2011, *ApJ*, **740**, 85
- Wevers, T., van Velzen, S., Jonker, P. G., et al. 2017, *MNRAS*, **471**, 1694
- White, R. L., Becker, R. H., Helfand, D. J., & Gregg, M. D. 1997, *ApJ*, **475**, 479
- Wilms, J., Allen, A., & McCray, R. 2000, *ApJ*, **542**, 914
- Wright, E. L., Eisenhardt, P. R. M., Mainzer, A. K., et al. 2010, *AJ*, **140**, 1868
- Yang, C.-W., Wang, T.-G., Ferland, G., et al. 2013, *ApJ*, **774**, 46
- Yang, J., van Bemmel, I., Paragi, Z., et al. 2021, *MNRAS*, **502**, L61
- Yang, Q., Shen, Y., Liu, X., et al. 2019, *ApJ*, **885**, 110
- Yang, Q., Wu, X.-B., Fan, X., et al. 2018, *ApJ*, **862**, 109
- York, D. G., Adelman, J., Anderson, J. E. J., et al. 2000, *AJ*, **120**, 1579
- Zabludoff, A., Arcavi, I., La Massa, S., et al. 2021, *SSRv*, **217**, 54